The Meteoritical Society

Meteoritics & Planetary Science 1–32 (2025)
doi: 10.1111/maps.70056

3D SR-μXCT analysis for lithology detection: Application to Ryugu sample A0159

Léna JOSSÉ[1]*, Zélia DIONNET[1], Alice ALÉON-TOPPANI[1], Rosario BRUNETTO[1], Andrew KING[2], Emmanuel GARDÉS[3], Eva HERIPRÉ[4], Damien LOIZEAU[1,5], Sasha CRYAN[1], and Kentaro HATAKEDA[6]

[1]Université Paris-Saclay, CNRS, Institut d'Astrophysique Spatiale (IAS), Orsay, France
[2]SOLEIL Synchrotron, Gif-sur-Yvette, France
[3]Laboratoire Magmas et Volcans (LMV), Université Clermont Auvergne, CNRS, IRD, Clermont-Ferrand, France
[4]Procédés et Ingénierie en Mécanique et Matériaux (PIMM), Arts et Métiers Sciences et Technologies, CNRS, CNAM, Paris, France
[5]Qualisat, Bièvres, France
[6]Institute of Space and Astronautical Science (ISAS), Japan Aerospace Exploration Agency (JAXA), Sagamihara, Japan

***Correspondence**
Léna Jossé, Institut d'Astrophysique Spatiale, Université Paris-Saclay, Orsay, France.
Email: lena.josse@universite-paris-saclay.fr

(Received 28 April 2025; revision accepted 15 September 2025)

Abstract–Extraterrestrial breccia samples are formed through impact-related processes that combine the fragments of distinct lithologies. As such, they are valuable indicators of the complex formation and evolution history of planetesimals in our solar system. Samples from asteroid (162173) Ryugu, returned to the Earth by the Hayabusa2 mission in December 2020, were characterized as breccias. The boundaries of mineralogical assemblages are typically drawn manually based on interpreted results from specific techniques, mostly performed on artificially produced 2D surfaces. This process inherently introduces subjectivity. Here, we present a semi-automated analytical method using synchrotron radiation micro X-ray computed tomography (SR-μXCT) data, called the Local Histogram method. It enables an unsupervised detection and 3D visualization of a few tens to hundreds of micrometer-sized lithologies showing sub-micrometer heterogeneities. We developed the method on a millimeter-sized Ryugu sample (A0159) in combination with a more traditional global grayscale threshold segmentation. In A0159, we report five distinct lithologies. They were confirmed and further characterized by an additional scanning electron microscopy (SEM) analysis on Xenon plasma-focused ion beam (Xe-pFIB) produced sections. Some lithologies show specific relationships with large fractures, while one is particularly enriched in sub-micrometer sulfides. A0159 is rich in carbonates and hosts the largest millimeter-scale dolomite vein seen on Ryugu.

INTRODUCTION

Asteroids are key entities for understanding the formation and evolution of the solar system. Numerical simulations on the formation and evolution of small bodies in the asteroid belt or near-Earth asteroids (NEAs) suggest that they formed through the fragmentation of larger, older parent bodies, followed by re-accretion (Bottke et al., 2005; O'Brien & Greenberg, 2005). Among them, 162173 Ryugu is a 900 m carbonaceous C-type NEA. This rubble-pile (Watanabe et al., 2019) asteroid was targeted in 2019 by JAXA's Hayabusa2 mission to collect surface and subsurface samples on February 21st and July 11th, respectively—5.4 g was brought back to the Earth in December of 2020.

According to Bischoff et al. (2006), breccias are a common rock type found in both differentiated and chondritic meteorites. Most meteorite breccias are thought to have formed either through surface or near-surface impact processes or by the accretion of fragmented parent body material. They consist of clasts (fragments) embedded in a fine-grained matrix. These clasts represent different lithologies (distinct mineralogical assemblages), each reflecting different formation and evolutionary processes. Consequently, breccias provide valuable insights into the geological evolution of planetary bodies in the solar system.

Previous 2D studies have shown that Ryugu samples can be described as breccias (Nakamura et al., 2023; Yamaguchi et al., 2023) with clasts ranging in size from 10 to 500 μm, according to Nakamura et al. (2023). The most common lithology is made of a phyllosilicate-rich matrix containing iron sulfides (pyrrhotite and pentlandite), carbonates (mainly breunnerite and dolomite), magnetite, and hydroxyapatite, all of which were formed through aqueous alteration processes (Mikouchi et al., 2022, 2025; Nakamura et al., 2023). Some lithologies show an enrichment in specific components such as carbonates or sulfides (Ito et al., 2022; Yamaguchi et al., 2023), whereas others were found to have remnant anhydrous minerals such as olivine, pyroxene, and amorphous silicates, providing information on the original ingredients that formed the Ryugu parent body (Aléon-Toppani et al., 2024; Brunetto et al., 2023; Kawasaki et al., 2022; Liu et al., 2022; Nakamura et al., 2023; Nakashima et al., 2023). The diversity in the petrology of adjoining fragments reflects the complexity involved in the formation and evolution of asteroid Ryugu and its parent body (Nakamura et al., 2022, 2023; Yamaguchi et al., 2023; Yokoyama et al., 2022). Thus, studying these lithologies in 3D and their interrelationships is essential for obtaining a better understanding of the evolutionary history of primitive asteroids and the processes that led to the formation of such breccia samples.

X-ray computed tomography (XCT) is a 3D nondestructive and non-invasive technique that can be used for the study of petrology and mineralogy. Its application to planetary materials dates back to the late 20th century and is now widely employed for the analysis of extraterrestrial samples as reviewed in Ebel and Rivers (2007) and Hanna and Ketcham (2017). Consequently, XCT has been extensively used to segment, quantify, and measure the shape and size of a sample or specific components (pores, chondrules, metallic phases, etc.) in meteorites or mission-returned samples (Dionnet et al., 2024; Ebel & Rivers, 2007; Friedrich et al., 2017; Friedrich & Rivers, 2013; Griffin et al., 2012; Hanna et al., 2022; Lindgren et al., 2015; Miyazaki et al., 2023; Nakamura et al., 2023; Noguchi et al., 2023; Tsuchiyama et al., 2021, 2024). However, there have been little XCT studies aimed at detecting and analyzing 3D mineralogical assemblages within brecciated samples.

Friedrich et al. (2014) studied an ordinary brecciated chondrite (NWA 7298) in which three distinct lithologies were identified. Their work digitally extracted XCT data into three subvolumes corresponding to each lithology, enabling an independent analysis of their petrofabric following the method described by Friedrich (2008). This approach established constraints on the evolutionary sequence of the lithologies, as well as on the intensity of the impacts that led to the formation of this breccia. More recently, Friedrich et al. (2025) focused on the clasts of the Ivuna meteorite, a CI chondrite which is considered the closest meteoritic class to Ryugu samples (Yokoyama et al., 2022). Following the methodology developed by Friedrich et al. (2022), they manually segmented individual clasts to analyze their volume, size, and shape and combined this with a porosity study to investigate the nature of brecciation.

To date, 3D analysis of clasts in CI-brecciated samples —or more generally, of distinct lithologies—has required a time-consuming preliminary manual segmentation of XCT data. This study presents a newly developed semi-automated data processing approach, the Local Histogram (LH) method, that extends XCT capabilities to detect distinct mineralogical assemblages within individual samples. In combination with the LH method, we applied a global grayscale threshold segmentation approach, referred to as the voxel-by-voxel (VV) method, for preliminary mineralogical description of the sample. This VV method was also used to constrain the mineralogy and physical properties of the detected lithologies.

Throughout this study, we use the terms "mineralogical assemblages" or "lithologies" to refer to distinct assemblages of minerals. This terminology is chosen to avoid confusion regarding their origin or formation process. In particular, the term "clasts" is intentionally avoided, as it typically implies fragmentation and mixing due to impact-related processes, which is not necessarily the case here. Our work was conducted on a millimeter-sized sample from Ryugu, with the goal of identifying distinct lithologies and visualizing them in three dimensions. These objectives aim to improve our understanding of the processes that led to the formation of those lithologies, which may be linked to brecciation, alteration events, or both that occurred on Ryugu or its parent body.

MATERIALS AND METHODS

Sample

For this study, we used the millimeter-sized Ryugu grain A0159 shown in Figure 1. This grain was collected

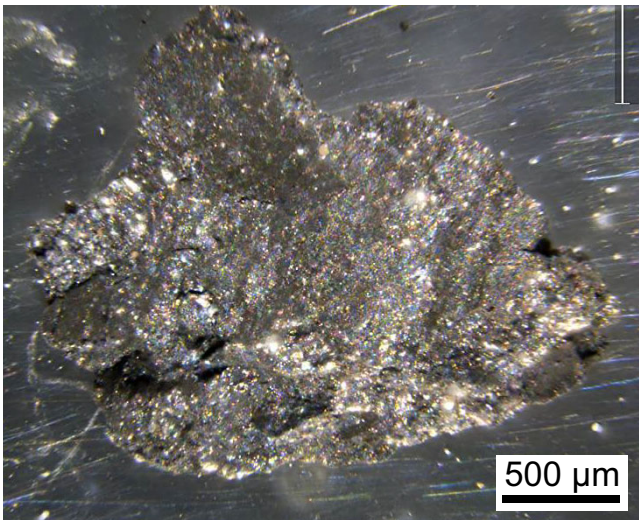

FIGURE 1. A0159 macroscope mosaic image taken at the Institut d'Astrophysique Spatiale after receiving the sample.

during the first touchdown (Chamber A) and measures 2.844 × 1.994 × 1.38 mm with a mass of 3.4 ± 0.07 mg (based on the JAXA catalog). A0159 represents 0.10 ± 0.002% of the total mass sampled by Chamber A (i.e., 3.237 ± 0.002 g) and is the 144th largest particle of 418 grains selected from Chamber A according to Yada et al. (2022), who analyzed the size distribution of particles larger than 1 mm. We chose A0159 because of its large size increasing our chances to find different lithologies.

Data

Preliminary Acquisition

A preliminary characterization of A0159 was carried out at the Curation Center of the Institute of Space and Astronautical Science (ISAS, Japan) using the MicrOmega instrument—a near-infrared (NIR) hyperspectral microscope—covering the spectral range of 0.99–3.65 μm with a pixel size of approximately 22 μm (Pilorget et al., 2022). This enabled the acquisition of the first NIR spectrum of the grain, as presented in Le Pivert-Jolivet et al. (2025). When A0159 arrived at the Institut d'Astrophysique Spatiale (IAS, France), it was imaged using a LEICA Z16Apo macroscope and MC190HD camera (Figure 1) while remaining in its sapphire well. During this first observation, we observed two grains of approximately 300 μm each, detached from the initial grain measuring several millimeters. The sample was likely fragmented during the transfer and travel to France due to the fragile nature of Ryugu samples (Yada et al., 2022). We carried out our study on the main and larger grain resulting from this fragmentation, which we will refer to as A0159 throughout this work. Then, a second near-IR hyperspectral characterization of A0159's surface was performed using the MicrOmega model instrument located at IAS, on the Planetary Terrestrial Analogues Library (PTAL) bench using conditions reported in Loizeau et al. (2020). This acquisition was performed on a different surface of A0159 than the one used during the preliminary characterization at ISAS, likely due to the grain having flipped during transport. We also performed a mid-IR hyperspectral imaging analysis in a nitrogen cell on the upper surface of A0159 using an Agilent Cary 670 Fourier transform IR (FT-IR) microscope equipped with a focal plane array detector (FPA) at SOLEIL synchrotron facilities (Saint-Aubin, France) in reflection mode. The spectral resolution was 8 cm^{-1}, in the range from 800 to 3900 cm^{-1}. We used a 15x objective and a 64 × 64 pixel FPA detector. Acquisition was limited to 64 scans. The pixel size was ≈5.5 μm for a field of view of 350 × 350 μm. A background spectrum was acquired on a gold surface before or after each analysis.

Synchrotron Radiation Micro X-ray Computed Tomography Data Acquisition

Synchrotron radiation micro X-ray computed tomography (SR-μXCT) data were acquired on the PSYCHE beam line (I03c) at the SOLEIL Synchrotron (King et al., 2016). The synchrotron was operated with a stored current of 100 mA. The photon source was a multi-pole wiggler, and an unfocused monochromatic beam was selected using a double crystal monochromator with a photon energy of 25 keV. The scan range was 360° and 3700 projections were acquired with an exposure time of 1300 ms each. For acquisition, the sample was deposited on the flat quartz (SiO_2) window delivered with the sample holder. No glue or tape was used to fix the sample to avoid contamination or changes in the physical properties.

Tomographic reconstructions were performed using the PyHST2 (Mirone et al., 2014). The data set consists of 1200 computed tomographic images (CT images), each saved individually in 32-bit TIFF format. Each CT image (or slice) has a size of 2304 × 1720 voxels (3D pixels) with a voxel size of 1.295 μm. Examples of slices are presented in Figure 2. Each voxel has a unique value, which is related to the local linear attenuation coefficient (LAC) and electron density of the sample. This attenuation coefficient depends on density and chemical composition making it theoretically calculable for a given component (e.g., mineral phase, chemical compounds, void) (Berger et al., 2010; Hanna & Ketcham, 2017). However, due to the technical configurations of SR-μXCT acquisition and reconstruction algorithms, the theoretical LAC often differs from the observed values (Tsuchiyama et al., 2005). As a result, theoretical LAC

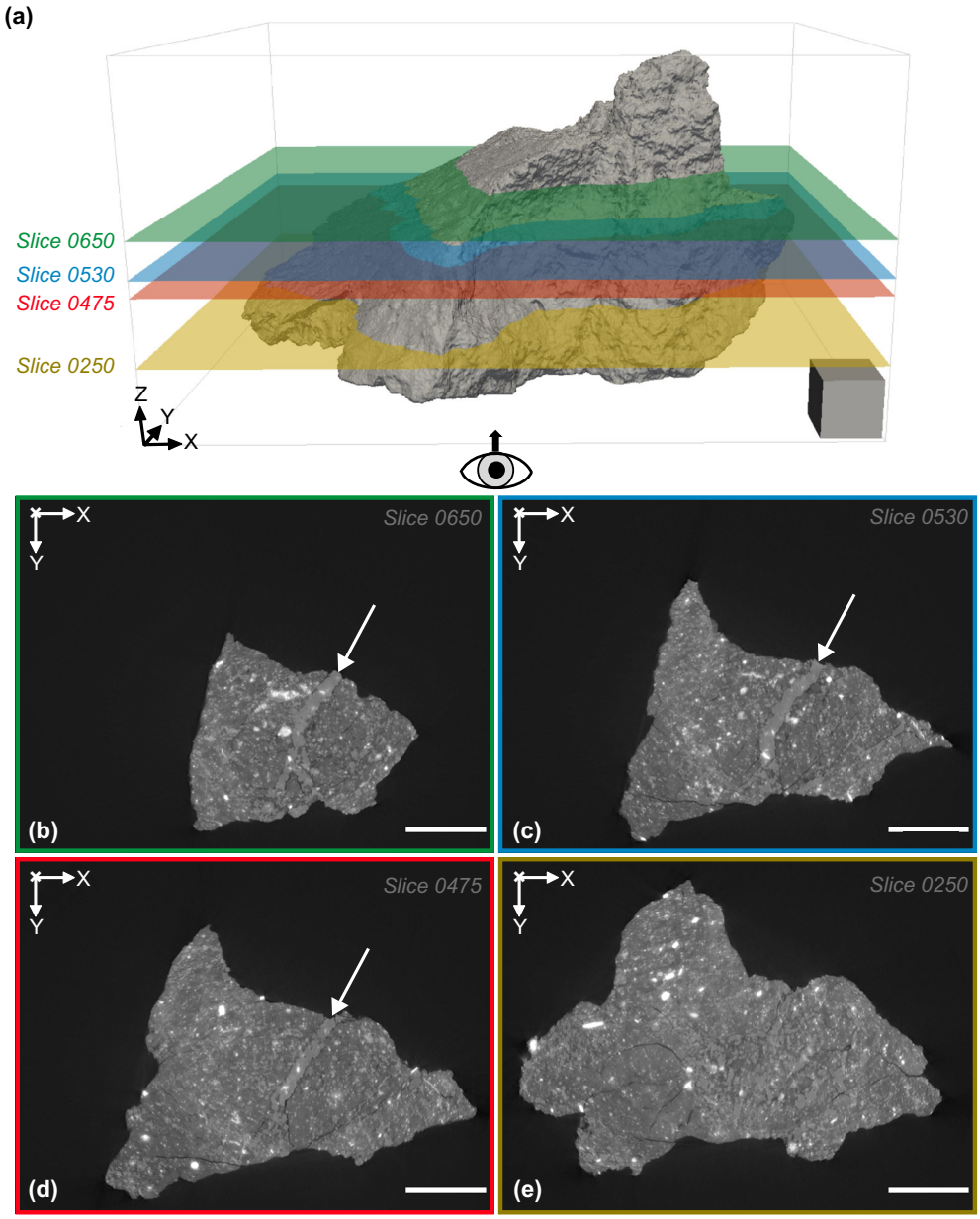

FIGURE 2. (a) A 3D model of A0159 in light gray with the position of the four particular slices, 0650, 0530, 0475, and 0250 in color using Tomviz software visualization. The scale box size is 250 μm, and the eye symbol indicates the direction of view for CT images of the corresponding slices shown in (b–e). White arrows indicate the carbonate vein. The reader is helped by the presence of an axial reference *X*, *Y*, *Z* in each panel. The scale bar is 500 μm.

values are not easily directly applicable to SR-μXCT data sets. In addition, each voxel typically contains a mixture of different components, meaning that its LAC value is a weighted average of all the components' attenuation coefficients contained within it (Bonse & Busch, 1996). This principle is known as the partial volume effect (PVE) (Ketcham, 2006). According to Bonse and Busch (1996), the voxel's intensity can be interpreted as a rough approximation of the average density of the materials it contains. A higher LAC value indicates stronger X-ray attenuation which generally corresponds to a denser mixture within the voxel. Voxel values are also affected by data blur, which can be modeled as a point spread function. This results in the voxel intensity being spread to neighboring voxels in a manner similar to a Gaussian smoothing kernel (Hanna & Ketcham, 2017; Ketcham, 2006; Ketcham & Mote, 2019). Consequently, sharp mineralogical phase boundaries become less distinct resulting in blurred CT images. The greater the contrast between two mineralogical phases (very different

LAC values), the easier it is to resolve fine details and identify small fine features. Conversely, when the LAC contrast is minimal, only larger structures can be clearly distinguished (Kyle & Ketcham, 2015). In our case, the spatial resolution is approximately 5 μm for features with the highest LAC value features.

Xenon Plasma Focused Ion Beam Section Preparation

To justify our 3D analysis and to further characterize our sample, we produced 2D sections using a Xenon plasma focused ion beam (Thermofisher Helios pFIB 5 CXe) at the Laboratoire Magma et Volcans (LMV) in Clermont-Ferrand (France). During manipulation, grain A0159 broke again into three fragments. Only two fragments were recovered, and the largest was delicately laid on a carbon tape fixed to an aluminum stub holder (Al-stub). On this larger fragment, two planar sections were prepared using 30 kV ion beam following a procedure similar to Nakamura et al. (2023). They were cut parallel to the Al-stub surface at different heights (Figure S2) to sample peculiar lithologies. For the largest section, Cut1, nicknamed *Pangea*, we used a beam current of 2500 nA. This section measures approximately 1 mm^2. For the smaller section, Cut2, measuring approximately 0.055 mm^2, the beam current was set first to 2500 nA and then to 500 nA.

Scanning Electron Microscopy Acquisition

Pangea and Cut2 sections were carbon-coated at the Muséum National d'Histoire Naturelle (MNHN), in Paris (France) using a LEICA ACE600, 2017 low vacuum coater to allow for SEM acquisition. The thickness of the carbon coating was estimated at roughly 20 nm. *Pangea* and Cut2 were observed using a TESCAN Bruker XFlash 62130 microscope located at the MNHN. The beam acceleration voltage and intensity were set to 15 keV and 1 nA, respectively, for both *Pangea* and Cut2. Backscattered electron (BSE) images and X-ray elemental mapping of *Pangea* were acquired with a 5% tile overlap parameter. Tiles have a size of 150 × 150 μm with a definition of 1000 × 1000 pixels. For Cut2, the field of view is 405 × 405 μm with a definition of 1000 × 1000 pixels.

DATA PROCESSING

VV Segmentation

A global grayscale threshold segmentation is a widely used method for analyzing XCT data, which requires assigning a voxel to a specific component based on its LAC value (Hanna & Ketcham, 2017; Jerram & Higgins, 2007). We initially applied this segmentation approach, referred to here as the VV method, to the A0159 SR-μXCT data set to (i) identify the major components within the sample, (ii) estimate their modal proportions, and (iii) provide an initial characterization of the heterogeneities in the mineralogical assemblages. Specifically, the last step enabled us to compare the mineralogical assemblages detected with the LH approach. For the following procedure, the sample was isolated from the surrounding environment (i.e., the background) to ensure that subsequent steps focus exclusively on components located within A0159.

Selection of Major Components

The first step involves the identification of components in A0159. The FT-IR analysis of the upper surface of A0159, shown in Figure 3, allowed us to identify two major components. First, a matrix-rich component, which has been previously shown to be dominant across Ryugu samples (Ito et al., 2022; Leroux et al., 2023; Nakamura et al., 2022; Tsuchiyama et al., 2024; Yamaguchi et al., 2023). This matrix is characterized by a mixture of saponite and serpentine phyllosilicates, sometimes including (Fe, Ni)-sulfide nano-inclusions (Ito et al., 2022; Nakamura et al., 2022; Noguchi et al., 2023; Yokoyama et al., 2022). In the matrix-rich FTIR spectrum (Figure 3c, shown in green), the band around 1000 cm^{-1} corresponds to the Si-O stretching mode of silicates (Beck et al., 2010, 2014; Brunetto et al., 2023; Dionnet et al., 2024). In all CT images, as shown in Figure 2b–e, the matrix component is characterized by relatively dark voxels abundantly present in the sample.

The second major component identified in A0159 is carbonate (Figure 3c, shown in yellow). Carbonates are identified by a band around 1500 cm^{-1} corresponding to an asymmetric stretching mode of CO_3^{2-} (Bishop et al., 2021). Figure 3b presents an intensity map of the carbonate band (the yellow dashed line in Figure 3c) within the red square on the LAC values 2D reprojection of the upper surface of A0159 (Figure 3a). Despite defocusing effects, the intensity map shows numerous carbonate features distributed as clusters, isolated grains, or in an arc-like pattern. By correlating these observations with the LAC values 2D reprojection (Figure 3a), carbonates can be localized on the SR-μXCT data set. They are characterized by slightly brighter voxels than the surrounding matrix, and due to their coarse-grained nature with well-delimited contours, carbonates are easily identifiable in CT images (Figure 2b–e). The carbonates were identified as dolomite (a Ca- and Mg-rich carbonate) based on near-infrared spectral analysis, following a similar approach to that of Loizeau et al. (2023). As shown in Figure S1, the absence of strong absorption features below 1.5 μm and the onset of the 3.3–3.5 μm absorption band at 3.31 μm support the presence of dolomite.

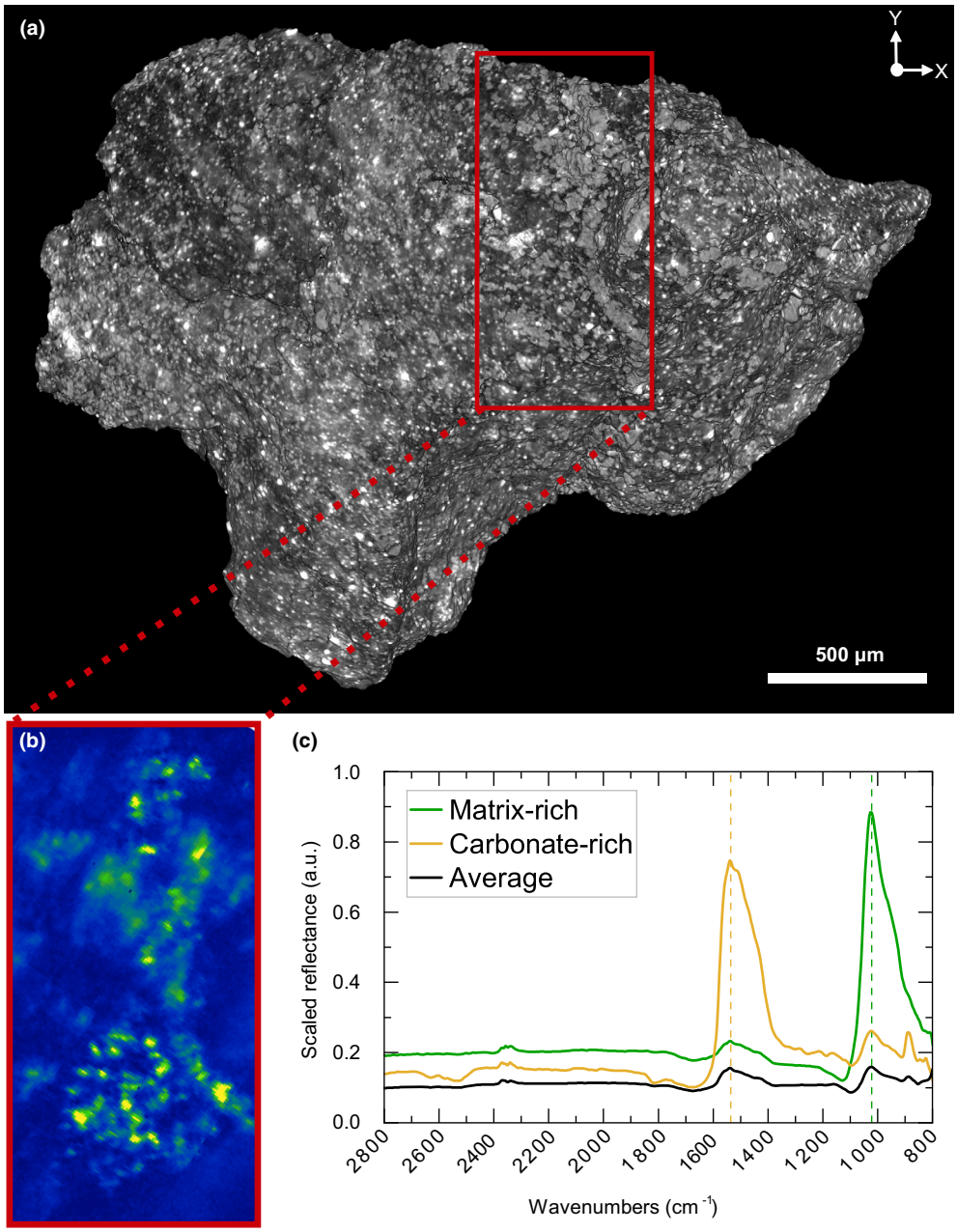

FIGURE 3. (a) A 2D reprojected view of the upper surface LAC values of A0159 on which was performed the infrared analysis. (b) Map of the intensity of the carbonate band (≈1500 cm^{-1}) in the area indicated by the red square in (a). Lighter pixels correspond to a carbonate-rich area and bluer pixels are for matrix-rich regions. (c) IR spectra from a matrix-rich (in green) and a carbonate-rich (in yellow) regions and the average spectrum of the upper surface of A0159 (in black). Dashed lines highlight strong bands at ≈1000 and 1500 cm^{-1} due to phyllosilicates and carbonates, respectively. Spectra have been shifted and rescaled to the total intensity.

Two minor components present on A0159 are also observed. The brightest voxels in the CT images (Figure 2b–e) correspond to dense material that strongly attenuates X-rays and can be classified as "opaque." Based on previous SEM analyses of Ryugu samples (Nakamura et al., 2022, 2023; Yamaguchi et al., 2023), the densest mineralogical phases are attributed mainly to sulfides (pyrrhotite and pentlandite) and oxides (magnetite). However, in our data, sulfides and oxides cannot be distinguished due to their overlapping LAC values, as in Tsuchiyama et al. (2002). On the contrary, black voxels relate to low X-ray absorption materials and are mainly present as elongated features resembling fractures in the CT images (Figure 2b–e). We

refer to this component as the low LAC values component, hereafter referred to as the LL component.

Other minerals (phosphate, olivine, etc.) (Nakamura et al., 2022, 2023; Noguchi et al., 2023; Yamaguchi et al., 2023) are either too rare or too small to be detected as a distinct component. Minor minerals, though likely present in the sample, were not considered in the VV segmentation.

Selection of LAC Intervals

The second step involves assigning LAC values to each component. Due to the effects of PVE and data blurring, attributing a unique LAC value to a given component is challenging. Selecting a range of LAC values is preferable and yields more accurate results. However, this interval selection is user dependent and directly influences the estimated modal abundance of each component, potentially representing a major source of uncertainty. Herein, we use multiple LAC intervals to (i) estimate the modal proportions of A0159 components and (ii) assess the impact of interval selection on modal abundance estimates. We defined three types of intervals:

1. Broad intervals—These provide a more inclusive segmentation by extending the selection close to the boundaries between different components (e.g., sample contours, fracture edges, or grain boundaries). This approach maximizes sampling but may lead to an overestimation of the components' relative abundances.
2. Narrow intervals—These represent a more restrictive segmentation, minimizing selection by focusing on the central region of each component. This method accounts for image blurring and the influence of neighboring components, leading to a potential underestimation of components' relative abundances.
3. Intermediate intervals—Used for the final segmentation, these provide a balance between inclusivity and specificity.

Together, the broad and narrow intervals establish upper and lower bounds for modal proportion estimates. The selected LAC value intervals for each component are summarized in Table 1. In some cases, LAC values could not be confidently assigned to a single component. These LAC values are therefore referred to as "mixing" components, and their abundance strongly depends on how strictly the other components' LAC intervals are defined. That is, the narrower the intervals used for the components, the more likely it is for voxels to fall into the "mixing" category. We do not consider the mixing component as a distinct component. Specifically, unassigned LAC ranges for the intermediate segmentation correspond to [3–3.5], [5–5.5], and [6.5–9].

TABLE 1. Linear attenuation coefficient (LAC) value intervals used for modal abundance calculations.

Components	Broad intervals	Narrow intervals	Intermediate intervals
Low LAC values	<3.25	<2.5	<3
Matrix	[3.25–5.5]	[3.75–4.75]	[3.5–5]
Carbonates	[5–7.25]	[5.75–6.5]	[5.5–6.5]
Opaques	>8	>10	>9

For each of the three segmentations (broad, narrow, and intermediate), the modal proportions of each component in CT images were calculated and averaged. This provided an intermediate value, along with upper and lower bounds for each component. The intermediate intervals were used for the VV segmentation presented in VV Segmentation Section.

LH Segmentation

While the VV segmentation is a basic approach for segmenting individual components and quantifying their relative abundances, the newly developed approach is designed to detect micrometer-scale mineralogical assemblages with reduced user intervention. The semi-automated data processing method, referred to as the LH segmentation, is applied to the initial SR-μXCT data set and thus, like the VV approach, enables the analysis of the entire 3D volume. However, it is more automated, as the user does not need to input predicted components or LAC values. The LH method consists of analyzing voxel frequency distributions across all LAC values within subvolumes obtained from the original data set. Then, the process of detecting specific mineralogical assemblages among those volumes is based on principal component analysis data reduction, which also requires minimal user intervention. The following sections detail these steps, which are summarized in Figure 4.

Transforming the SR-μXCT Data Set into Local Mineralogical Assemblages

Since most LAC values can be attributed to specific components, a group of voxels within a given volume that exhibits different LAC values can reflect local variations in the mineralogical assemblages. In this study, such a volume is referred to as a *macrovoxel*, defined as a cube with user-specified dimensions. Creating macrovoxels involves partitioning the SR-μXCT data set in three dimensions (X, Y, and Z) based on the chosen macrovoxel size. This partitioning generates a new data set.

Fragments in Ryugu samples range from 10 to 500 μm (Nakamura et al., 2023). After evaluating different macrovoxel sizes, we found that a cube size of 25 × 25 × 25 voxels (≈33 μm^3) is best for our analysis.

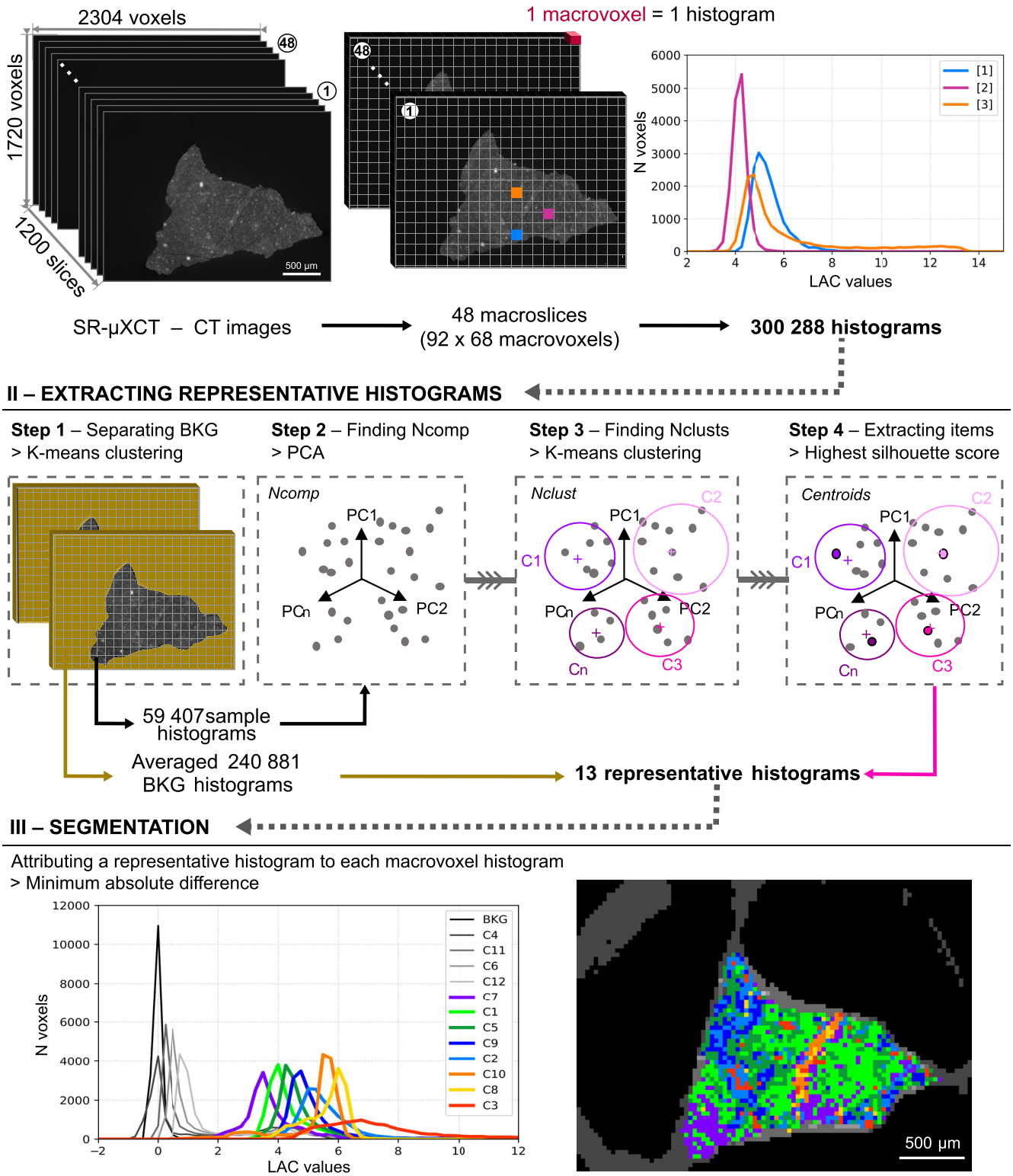

FIGURE 4. Schematic illustration for the Local Histogram method separated into three major steps: transforming the data set, extracting the representative assemblages, and segmentation. SR-µXCT, synchrotron radiation micro-X-ray computed tomography; CT images, computed tomography images; N voxels, number of voxels; LAC, linear attenuation coefficient; BKG, background; Ncomp, number of principal components (PC*n*); PCA, principal component analysis; Nclusts, number of clusters (C*n*).

Within this macrovoxel size, smaller lithologies are incorporated into a larger scale mineralogical assemblage while larger lithologies result in multiple and adjacent macrovoxels that are similarly segmented.

We used a Python script to transform the original data set into macrovoxels (Figure 4I). Since 2304 (X dimension) is not divisible by 25, the 1200 SR-μXCT TIFF images (slices) were reduced (e.g., X reduced to 2300) to obtain an integer number of macrovoxels in the three dimensions. We crop our data set symmetrically by trimming the empty margins surrounding the sample. For each set of 25 SR-μXCT TIFF slices (Z-axis), a new file, referred to as a *macroslice*, was created with dimensions of 92 × 68 (92 macrovoxels in X and 68 in Y). This step transformed the original SR-μXCT data set consisting of 1200 slices of 2304 × 1720 voxels into a data set of 48 macroslices each of size 92 × 68 macrovoxels (300288 total macrovoxels).

Each macrovoxel containing 15,625 voxels was represented by a histogram showing the distribution of voxel LAC values. The histogram parameters were optimized for resolution and processing time: the open source software, ImageJ (Schneider et al., 2012), provided minimum and maximum LAC values corresponding to the CT images, and the bin size was user defined. While small bin sizes improve histogram resolution, they significantly increase processing time (e.g., 214 ms per histogram for a bin size of 0.1 compared to 24 ms for a size of 1). To balance detail and efficiency, we selected a bin size of 0.25 over an LAC range from −3 to 30. This resolution captures differences between histogram peak centers (Figure 4I) while keeping computational time minimal for our large A0159 data set (17 GB). Each macrovoxel is thus described by 132 bins, corresponding to specific LAC intervals and their associated voxel counts. Finally, the 48 macroslices containing 92 × 68 histograms were saved as text files.

Representative Mineralogical Assemblages Retrieval and Segmentation

To identify the representative mineralogical assemblages in A0159 using the 300,288 histograms defined above, we applied a four-step procedure (Figure 4II). The analysis was performed using the open-source software Quasar (Toplak et al., 2017, 2021), which facilitated data manipulation and analysis.

Step 1 involved separating the background histograms (BKG, those corresponding to macrovoxels sampling regions outside the grain) from those within the sample (sample histograms). This was achieved by unsupervised clustering using a k-means algorithm. As a result, sample A0159 was reduced to 59,407 histograms, while the 240,881 background histograms were averaged into a single representative histogram.

Step 2 involved reducing the dimensionality of the data set (59,407 histograms × 132 bin values) using principal component analysis (PCA). This transformed the data set into a new coordinate space defined by N components (Ncomp), chosen to capture at least 95% of the data set's total variability. As a result, the histograms were converted into new items, each characterized in the Ncomp coordinate space. For sample A0159, this process yielded 11 components (Ncomp = 11).

Step 3 involved applying a second k-means clustering algorithm to the PCA-transformed data set to determine the optimal number of representative histograms (Nclust). This step identified the ideal number of clusters to best describe the variability of the mineralogical assemblages. The optimal Nclust was determined using silhouette scores, with higher scores indicating better clustering. For sample A0159, the optimal Nclust corresponded to 12.

Step 4 involved extracting a unique representative histogram for each cluster by evaluating the silhouette coefficient of each item. A higher silhouette coefficient indicates a closer proximity to the cluster center (centroid). Histograms with the highest silhouette coefficients in each cluster (analogous to cluster endmembers) were selected as the representative histograms.

The four-step procedure resulted in a set of 13 representative histograms: 12 derived from the sample and 1 corresponding to the background. Additionally, each histogram was characterized using two parameters: the LAC value at the peak maximum and the standard deviation of a Gaussian function fitted to that peak. The peak center reflects the dominant attenuation coefficient, while the standard deviation indicates the diversity of materials associated with the histogram. These representative histograms served as a reference for the following segmentation procedure (Figure 4III).

Segmentation consisted of assigning each 300,288 macrovoxel histogram to a representative histogram (labeled C1–C12 and BKG in Figure 4III) using a Python script. The absolute difference between each macrovoxel histogram and each representative histogram was computed by summing, bin-by-bin, the differences between the values of the two histograms. Each macrovoxel histogram was then assigned to the representative histogram that provided the lowest absolute difference. Color coding the representative histograms thus enabled the visualization of the mineralogical assemblage distribution in A0159 (Figure 4III). This segmentation step quantified the number of macrovoxels assigned to each mineralogical assemblage and allowed for the calculation of their proportions and volumes. To estimate the uncertainties associated with the relative proportion and volume, we identified and excluded isolated macrovoxels—those lacking direct adjacent macrovoxels of the same assemblage—and recalculated the

TABLE 2. Estimated modal abundances (vol%) of major components for the three intervals.

Intervals	Low LAC values	Carbonates	Matrix	Opaques	Mixing
Broad	1.5	28.8	64.6	2.9	2.2
Narrow	0.4	15.8	33.4	0.9	49.5
Intermediate	0.9	22.7	46.6	1.6	28.2

Note: Low LAC values component only count for voxels within the sample, not the background.
Abbreviations: LAC, linear attenuation coefficient.

macrovoxel counts, modal proportions, and volumes accordingly. These isolated macrovoxels may correspond to false or ambiguous mineralogical detections due to highly localized heterogeneities. We used the average of both calculations (with and without isolated macrovoxels) to quantify the associated uncertainties using the standard deviation.

RESULTS

VV Segmentation

Modal Proportion and Distribution of the Components

Table 2 presents the modal abundances calculated using the three different intervals (broad, narrow, and intermediate), emphasizing their dependence on the selection of LAC intervals. This dependence is further illustrated in Figure S3, which shows the selection of carbonates using the two extreme intervals on slice 0475. The selection of a broad LAC interval for the carbonate component was guided by the segmentation of the vein structure attributed to carbonates and indicated by the white arrow in Figure S3. We thus expanded the LAC interval to maximize the selection of this vein. The result (Figure S3) shows that the vein appears to have been correctly segmented, although we suspect an overselection of the carbonate component in the rest of the sample. In contrast, with a narrower LAC interval (Figure S3), based on sampling the core of the vein, the vein is only partially segmented. From the broad to narrow interval, the relative proportion of carbonate varies significantly, decreasing from approximately 30 to 15 vol% (Table 2). For the intermediate interval, the carbonate content is roughly 25 vol%. We note that the ratios between different components remain relatively stable across the different segmentation intervals. Therefore, we use component ratios rather than absolute modal abundances for interpreting the results.

Figure 5e–h shows that the VV segmentation results applied to the slices 0650, 0530, 0475, and 0250 that are shown in Figure 5a–d. These VV-segmented images reveal that all the components are heterogeneously distributed throughout sample A0159. The *matrix* is the main component (Table 2), but its heterogeneous distribution defines regions that are locally enriched or depleted in matrix material, represented in green in Figure 5e–h. *Carbonate* is the second most abundant component in A0159 (Table 2), with a matrix-to-carbonate ratio of ≈2 within the intermediate interval. In Figure 5e–h, carbonates appear in yellow and exhibit various morphologies: Some appear as well-defined, round, or irregular grains (white dotted arrows, Figure 5e–h), while others appear as part of an extended structure associated with the vein (white solid arrow, Figure 5e–g). In slice 0475 (Figure 5g), the vein measures approximately 850 × 100 μm and nearly bisects sample A0159, as on upper slices 650 and 530 (Figure 5e,f). Regions enriched in carbonates appear to be depleted in the matrix component. The carbonate component is discussed in greater detail in Carbonate Component in 3D Section, which focuses on its 3D distribution. The *opaque* component is the third most abundant component (Table 2) and it primarily occurs as coarse-grained minerals. These opaques are a few tens of microns in size and are either surrounded by the matrix or embedded in the carbonate component (Figure 5e–h). Slice 0250 (Figure 5h) shows regions enriched in large (≈50 μm) opaque grains, which are represented in red. Finally, the *LL* component is the least abundant (Table 2) and is represented by black voxels within the sample (Figure 5e–h). This component mostly appears as thin elongated structures, interpreted as fractures, although we also observe rounded or irregular *patches*. This component will be further analyzed in The 3D Low LAC values (LL) Component Description and Distribution Within Lithologies Section through its relationship with 3D lithologies.

The results from VV segmentation show the pronounced heterogeneity of the major components in A0159, as well as enable the independent visualization of each component. In the following section, we focus on the carbonate component, which is highly abundant in A0159 and exhibits a distinctive vein-like structure.

Carbonate Component in 3D

Figure 6 displays different perspectives of the 3D distribution of the carbonate component within sample A0159. The continuity of the carbonate vein previously detected in Figure 5e–g is clearly visible. Figure 6a shows that the vein is curved from the top view and nearly crosses the grain along the Y-axis. Along this axis, the vein measures from 750 μm to about 1 mm depending on its location in the sample. In Figure 6b, a side view reveals that the vein extends roughly 1 mm along the *Z*-axis and is approximately 100 μm wide along the *X*-axis. The vein appears discontinuous on the *Z*-axis,

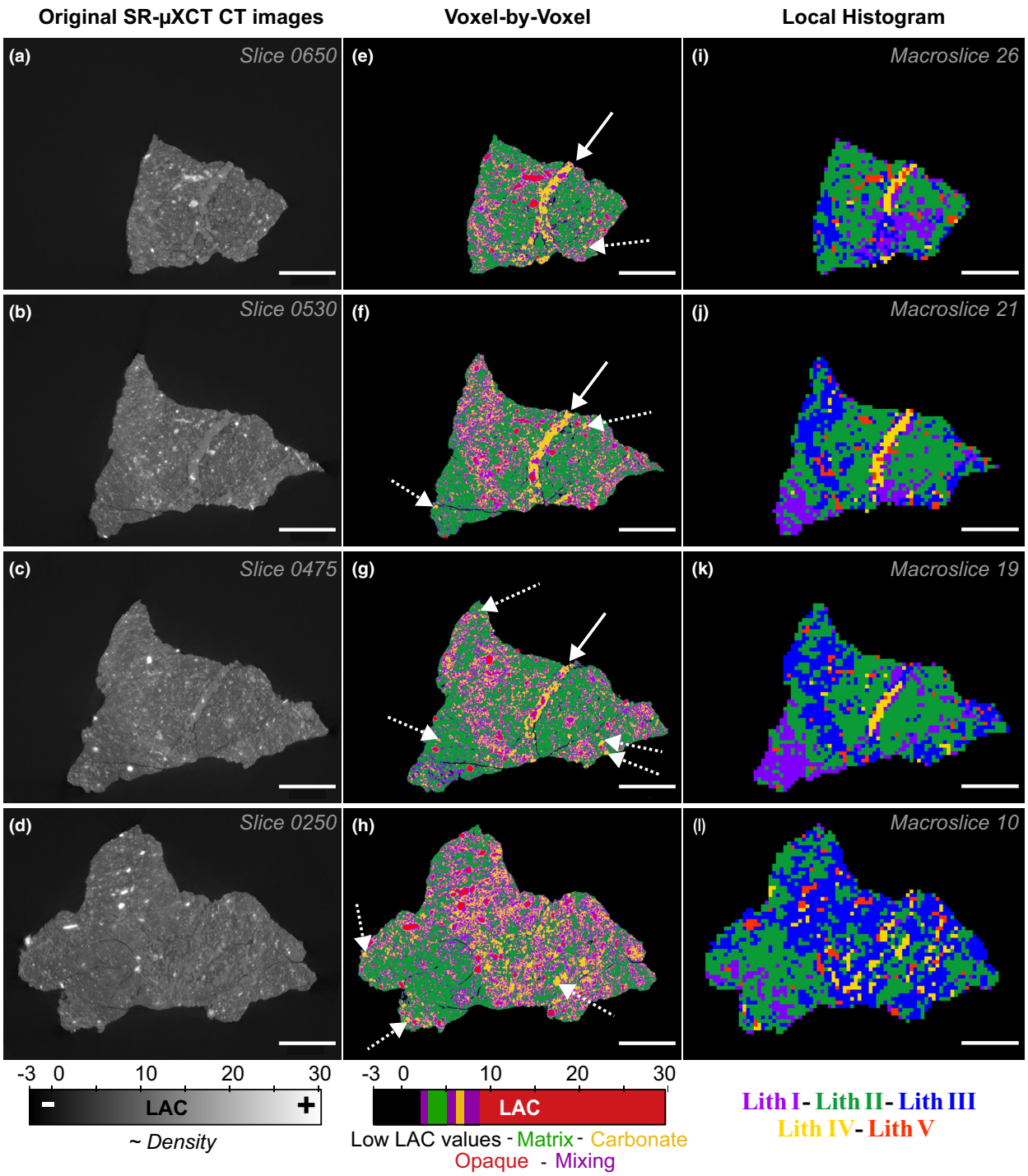

FIGURE 5. (a–d) Tomographic slices (0650, 0530, 0475, 0250) from the original data set of sample A0159. Voxel grayscale values correspond to the linear attenuation coefficient (LAC), which is approximately related to material density: the higher the LAC, the denser the component. (e–h) Voxel-by-voxel segmentation results based on LAC values for the corresponding slices. Components were segmented using the following LAC ranges: low LAC values (<3; shown as black voxels within the sample), matrix (3.5–5; green), carbonates (5.5–6.5; yellow), and opaques (9–30; red). Intermediate values (3–3.5), (5–5.5), and (6.5–9) were assigned to a "mixing" category (purple). Voxels with LAC <3 located outside the sample were considered as background. Solid white arrows indicate the carbonate vein; white dotted arrows point to scattered carbonates. (i–j) Segmentation of lithologies (Lith. I–V) obtained using the Local Histogram method on macroslices 26, 21, 19, and 10 containing slices 0650, 0530, 0475, and 0250, respectively. Scale bar is 500 μm.

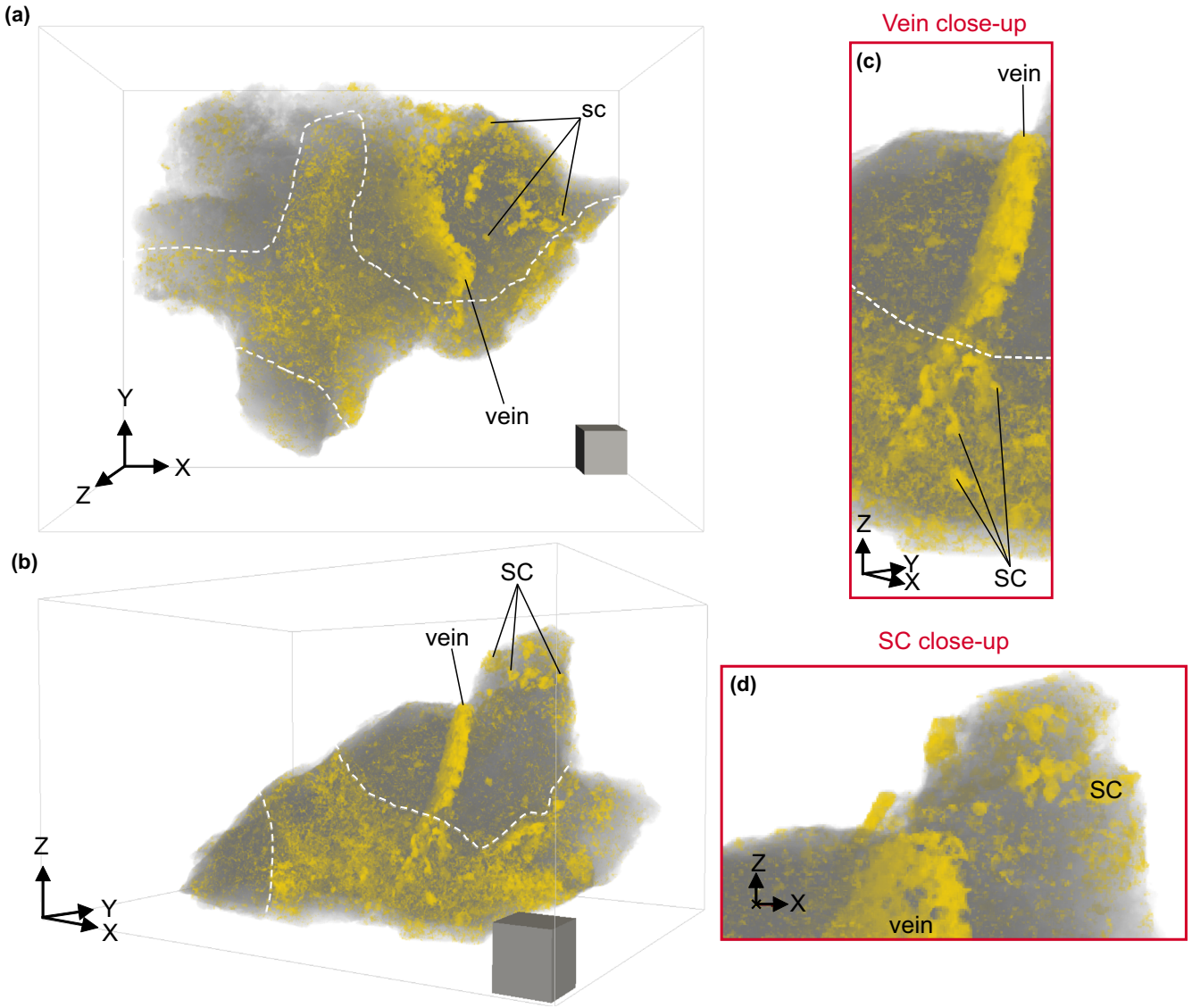

FIGURE 6. Carbonate component (in yellow) combined with the shape model of A0159 (in gray) using Tomviz software. The intensity color depends on the density of the voxels along the line of sight. (a) A 3D visualization from the top, along the *Z*-axis, and (b) from the side. (c, d) Close-ups showing vein structure and a scattered carbonates (SC)-rich region, respectively. White lines separate different regions where carbonates are either abundant or relatively absent. The scale box size is 250 μm.

a region highlighted by the close-up (Figure 6c). At one of its extremities, the vein splits into well-defined carbonate grains, which we refer to here as *scattered carbonates* (SC).

SC are roundish or irregular shaped grains in Figure 6 and, unlike the vein, they do not exhibit preferred orientation. SC are identified by a higher density of segmented carbonate voxels (represented in more intense yellow in Figure 6) and exhibit clear boundaries. They typically range from a few tens to several hundreds of micrometers in size. Some regions, such as the elevated bump feature on the upper right side of the grain (Figure 6b and close up Figure 6d), appear particularly abundant in SC.

The dotted white lines in Figure 6a–c indicate a boundary between two regions. A globally more yellow tone across one region reflects its higher carbonate concentration relative to the other. However, unlike the SC, carbonate detections in this more yellow region are diffuse, lacking well-defined grain boundaries or specific morphologies. A carbonate-depleted region, observed on either side of the carbonate-rich region, contains most of the vein. In its lower extension, however, the vein splits into SC within the carbonate-rich region (Figure 6b,c).

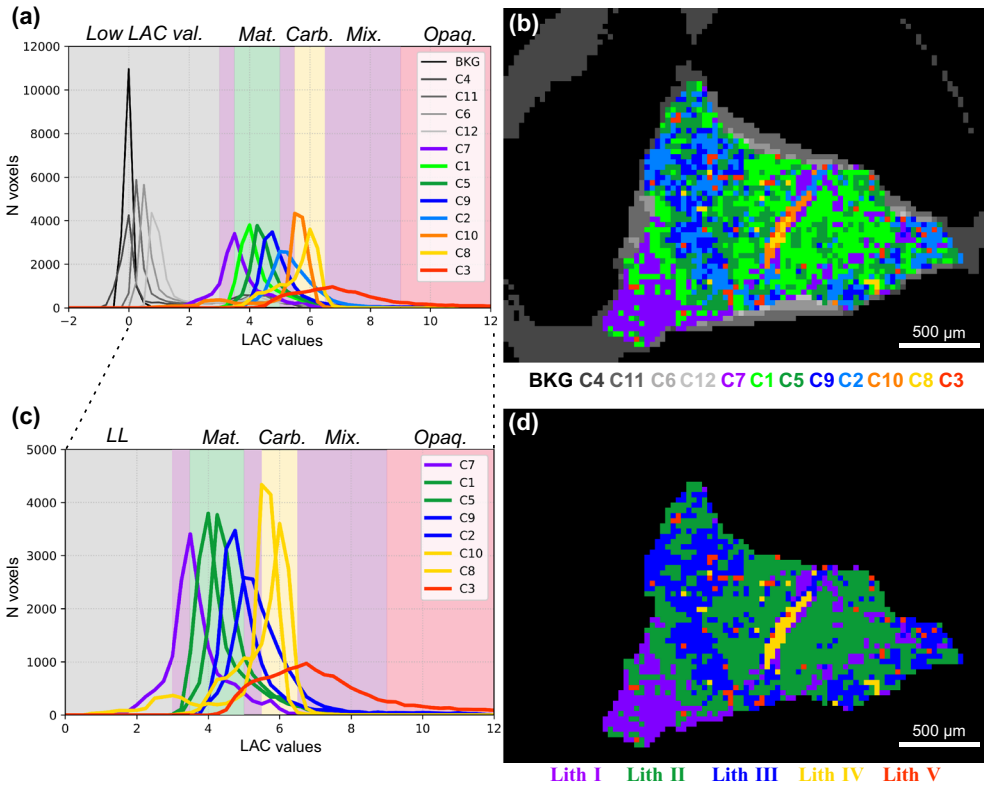

FIGURE 7. (a) Representative histograms retrieved using the Local Histogram (LH) method overlapped with the intermediate intervals used for the Voxel-by-Voxel segmentation. (b) Result of the LH segmentation on the macroslice 19 using the representative histograms shown in (a). (c) Zoom of (a) showing results of the additional processing step for sample A0159, in which representative histograms are grouped into lithologies. (d) Result of the LH segmentation on the macroslice 19 using the grouped histograms of (c).

This carbonate-enriched region will be further explored in Matrix, Carbonate, Phosphate, and Opaque Section.

In summary, a 3D analysis of the carbonate component derived from the VV segmentation reveals three distinct occurrences of carbonates: (i) a millimeter-sized vein, (ii) grains with roundish or irregular morphologies ranging from tens to hundreds of micrometers (SC), and (iii) larger regions enriched in carbonates. Other regions are depleted in carbonates.

LH Segmentation

The VV segmentation approach enabled the identification of distinct regions enriched or depleted in a given component (Figures 5e–h and 6). However, the identification of these regions relies on the user's expertise and consequently introduces subjectivity in the detection and delineation of mineralogical assemblages—an issue that the LH segmentation method overcomes.

Representative Histograms and Number of Lithologies

Figure 7a,b presents representative histograms derived from the LH method and the segmentation result for macroslice 19, which includes slice 0475. In Figure 7a, we identified two groups of histograms: One containing five histograms whose main peak is centered at lower LAC values (LAC <2) and another containing eight histograms which peak at higher LAC values. In the segmentation (Figure 7b), macrovoxels corresponding to the first group are located around or at the edges of the sample while those in the second group are located within the sample. Moreover, some mineralogical assemblages that are segmented differently exhibit spatial correlation. For instance, the distribution of C10 and C8 macrovoxels in Figure 7b clearly highlights the observed carbonate vein. Based on this spatial correlation, we performed an additional step to group representative histograms together to form unique mineralogical assemblages, referred to as *lithologies* hereafter. This additional step improved the 3D visualization of the mineralogical assemblages of A0159 using the open-source software Tomviz (Schwartz et al., 2022) and facilitated the interpretation and discussion of the results. Grouping of representative histograms was guided by (i) the spatial distribution of the macrovoxels from the initial LH segmentation (e.g., Figure 7b), (ii) the histogram

TABLE 3. Representative histogram parameters and final assignment.

Representative histograms	PC	SD	Attributed lithologies
BKG	−0.03	0.14	BKG
C4	−0.05	0.19	BKG
C11	0.29	0.14	BKG
C6	0.53	0.16	BKG
C12	0.87	0.19	BKG
C7	3.5	0.42	Litho I
C1	4.0	0.35	Litho II
C5	4.39	0.37	Litho II
C9	4.77	0.4	Litho III
C2	5.29	0.6	Litho III
C10	5.64	0.26	Litho IV
C8	5.97	0.37	Litho IV
C3	6.7	1.37	Litho V

Abbreviations: BKG, background; PC, peak center; SD, standard deviation.

parameters from the 13 representative histograms presented in Table 3, and (iii) the intermediate LAC intervals of the major components found through previous VV analysis and visualized as shaded regions on the histogram plots (Figure 7a,c).

In Figure 7a, four histograms (C4, C11, C6, C12, from dark to light gray) resemble the BKG histogram (black). These histograms contain a high proportion of very low LAC values (LAC <2), with peak centers and standard deviations close to those of the BKG histogram (−0.03 and 0.14, respectively; Table 3). Their macrovoxels are spatially located near or at the sample edges (Figure 7b), indicating that they are probably sampling background/void (surrounding air) voxels. Histograms C4, C11, C6, and C12 were thus classified as the background.

The remaining eight representative histograms (C7, C1, C5, C9, C2, C10, C8, and C3) in Figure 7a exhibit varying shapes and peak centers. Among them, C7 peaks at 3.5 and exhibits a standard deviation of 0.42 (Table 3). Its overlap with the low LAC values defined by the VV method (shaded in gray in Figure 7a,c) suggests that C7 contains a higher proportion of the LL component compared to the others. In the LH segmentation (Figure 7b), C7 macrovoxels are highly localized, particularly in the lower left section of the sample. We therefore classified C7 as a distinct lithology (Lithology I, Figure 7c,d).

Histograms C1, C5, and C9 likely present a higher matrix proportion as inferred from their overlap with the matrix interval (Figure 7a). They also have similar peak centers (4.0–4.77) and standard deviations (0.35–0.4) as shown in Table 3. In contrast, C2 differs in shape both with a higher peak center (5.29) and standard deviation (0.6). Its broad peak overlaps both the matrix and carbonate intervals (Figure 7a).

In the LH segmentation (Figure 7b), C1 and C5 macrovoxels are spatially correlated, especially around the vein where they dominate. Given their similar peak centers (4.0 and 4.35) and standard deviations (0.35 and 0.37; Table 3), we grouped C1 and C5 histograms into Lithology II (Figure 7d). Although C9 exhibits a similar peak center and standard deviation as C1 and C5, its macrovoxels are often adjacent to those of C2, both mainly located around the central region of the sample (Figure 7b). We therefore grouped C9 and C2 into Lithology III (Figure 7c,d).

Histograms C10 and C8 largely overlap the carbonate interval (Figure 7a), consistent with their macrovoxels aligning with the carbonate-rich vein location previously identified in Figure 5e–g. Their peak centers (5.64 and 5.97) are closely spaced, and C10 exhibits a small standard deviation (0.26), indicating limited component diversity and a high proportion of a dominant component—likely carbonate (Figure 7a). We grouped C10 and C8 as Lithology IV (Figure 7c,d).

Histogram C3 has the widest distribution with a standard deviation of 1.37, reflecting a mixture of light and dense materials. With its highest peak centered at 6.7, C3 contains more opaque and mixed components, particularly in the [6.5–9] interval (Figure 7a). We therefore classified C3 as a distinct lithology referred to as Lithology V (Figure 7c,d).

Figure 7c shows the final histogram grouping, where the eight representative histograms from within the sample are color-coded based on the five lithologies. This classification was used to segment the 48 macroslices, as also shown for macroslices 26, 21, 19, and 10 containing the slices 0650, 0475, 0530, and 0250, respectively (Figure 5i–l).

Lithology Distribution in 3D

Segmentation of the 48 macroslices enabled 3D visualization of the lithologies in A0159 (Figure 8a,b), with corresponding 3D model views in Figure 8c,d to aid interpretation. Table 4 summarizes the characteristics of each lithology, including macrovoxel counts, relative abundance, total volume, 3D spatial distribution, and relationship with the LL component detected through the VV method.

Lithology I is the third most abundant representing approximately 11% of sample A0159 (Table 4). As illustrated by Figures 8 and 5j,k, its macrovoxels are mainly concentrated along one edge of the sample forming a 500 μm wide zone. Additional Lithology I macrovoxels are present on the upper surface of the sample near the vein (Figures 8a and 5i–k).

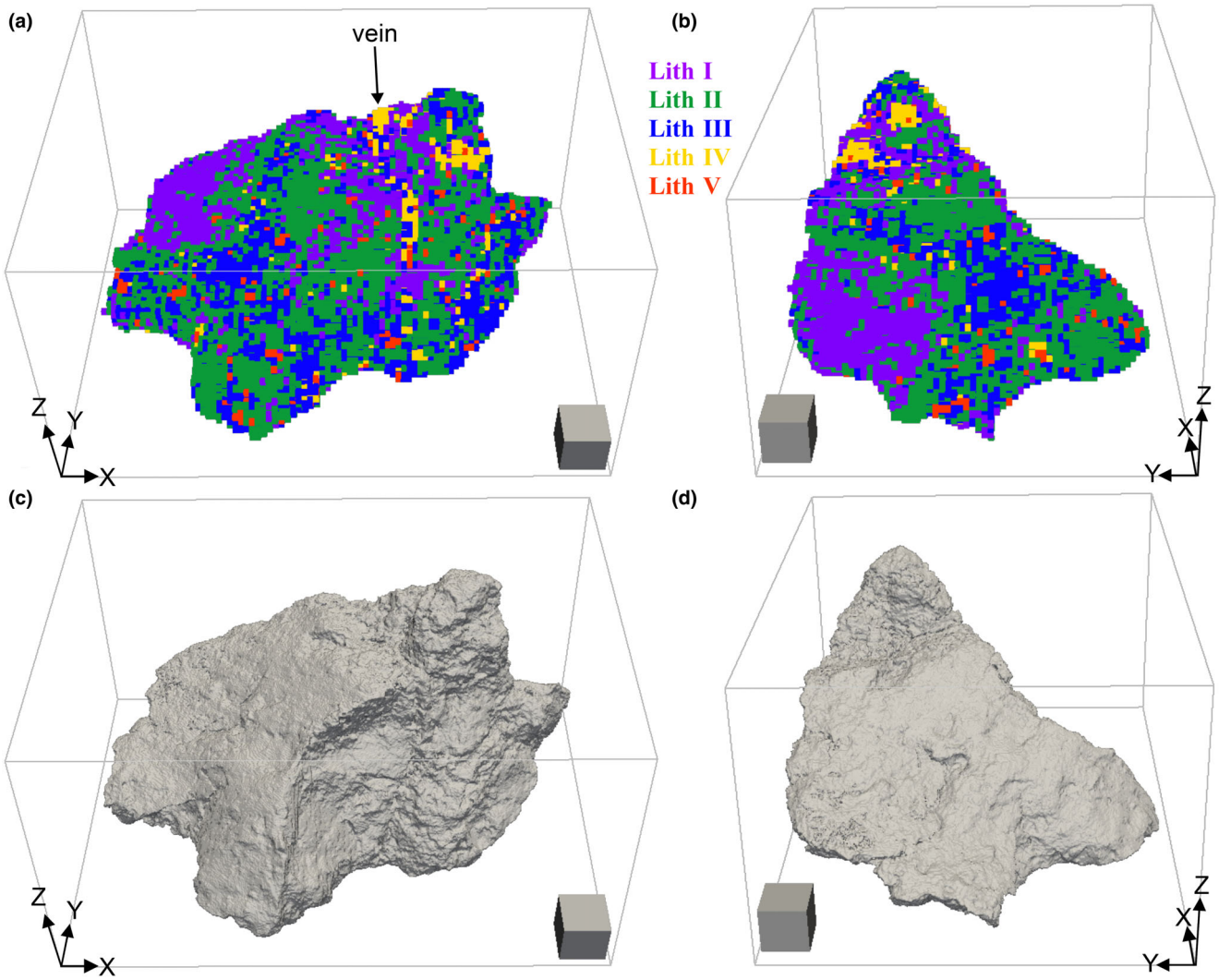

FIGURE 8. (a) and (b) Two different views of sample A0159 illustrating the distribution of lithologies (Lith. I–V) based on the Local Histogram method. (c) and (d) Shape model generated using the Voxel-by-Voxel method, oriented identically to (a) and (b). The *X*, *Y*, and *Z* axes are shown to facilitate 3D visualization. The scale box size measures 250 μm.

Lithology II is the most abundant, comprising ≈45% of A0159 (Table 4). Some regions consist entirely of Lithology II, with areas of approximately 250 μm^2 at the sample surface (Figure 8a,b) and up to 500 μm^2 in its interior (Figure 5i–l). Lithology II frequently surrounds Lithology I, and larger regions contain a mix of Lithology II and Lithology I or III (Figures 8a,b and 5i–l).

Lithology III is the second most abundant and accounts for roughly 35% of the sample (Table 4). It mainly co-occurs with Lithology II macrovoxels, occupying the central and lower regions of A0159 (Figures 8a and 5j–l). This distribution extends along the *X*- and *Y*-axes (Figure 8a,b), spanning several millimeters. Smaller isolated regions (≈250 μm^2) are also segmented as Lithology III only (Figures 8b,d and 5j–l). A few macrovoxels appear near Lithology IV (Figure 8a) and occasionally near Lithology I (Figure 8a,b).

Lithology IV is rare (roughly 5% of the sample, Table 4) and highly localized, typically appearing in the same regions as the vein and large scattered carbonates (Figures 8a and 5i–l). It is absent from the Lithology I-dominated region and only sporadically present everywhere else in the sample (Figures 8a,b and 5i–l).

Lithology V has a similar abundance (≈4%, Table 4) but is distributed differently than Lithology IV. Unlike Lithology V, macrovoxels are sparsely dispersed throughout the sample, particularly in millimeter-sized regions containing Lithologies II and III. Occasionally, Lithology V forms small clusters (<250 μm^2), especially apparent in Figure 5i,j,l.

TABLE 4. Lithologies of A0159 description.

Litho.	MV count	Total vol. (μm^3)	Rel. abun. (%)	3D description	Link with low LAC values components
LI	5283 ± 1027	574 ± 37	11 ± 1.1	Localized (500 μm-sized region), surrounded or combined with LII	Contains a lot of patches and fractures, is often surrounded by fractures
LII	22,347 ± 933	929 ± 13	45 ± 2.2	Predominant, localized or combined with LI or LIII	Rare patches, is often surrounded by fractures
LIII	17,408 ± 1400	855 ± 23	35 ± 0.4	Small (250 μm-sized) localized, or large (mm-sized) regions combined with LII (and LV)	Fractures and patches are rare
LIV	2531 ± 501	449 ± 30	5 ± 0.5	Carbonate vein and SC-rich region mainly, rare in LI and LIII	Surrounded by fractures
LV	1828 ± 636	401 ± 47	4 ± 1.0	Sparse or small regions (<250 μm)	n.a
Total	49,397 ± 4497	3207 ± 150			

Note: Count, volume, and proportion are rounded to the nearest percent; uncertainties for proportion are reported with one decimal place to reflect the precision of the estimates.

Abbreviations: LAC, linear attenuation coefficient; Litho, lithologies; MV, macrovoxels; n.a., non-available; Rel. abun., relative abundance; SC, scattered carbonates; vol, volume.

The 3D LH segmentation reveals distinct spatial distributions of the identified lithologies. It highlights regions of varying scale, from small zones dominated by a single lithology (e.g., Lithology I- or II-rich) to millimeter-scale regions where Lithologies II, III, and occasionally V are present at the same time.

The 3D Low LAC Values (LL) Component Description and Distribution Within Lithologies

We combined the segmentation of the low LAC values (LL) component with the segmentation of lithologies in order to further characterize this component and its relationship with the detected lithologies. Figure 9a shows the LH segmentation results for roughly half of sample A0159 obtained by stacking the first 20 macroslices. Superimposed on the lithologies is the LL component identified using the VV method spanning slices 0000 to 0484. The CT image of slice 0484 is displayed in Figure 9b.

In Figure 9a (and close-up Figure 9c), the LL component appears as thin, elongated features consistent with fractures. In the CT images (Figure 9b,d), these fractures appear very dark akin to the air/void surrounding the sample, suggesting an absence of material. The width of the fractures can vary but is generally around 10 μm. The length ranges from about 50 μm (Fracture F, Figure 9a,b) to 550 μm (Fracture B; Figure 9a–d). The red dashed square in Figure 9a highlights a region rich in patches (outlined in white in close-up Figure 9c). The patches identified have been mapped on the CT image (Figure 9d). Patches range from 5 to 60 μm in length and, like fractures, are heterogeneously distributed.

Fracture A, about 750 μm long, propagates through the sample in the Z direction and its location coincides with the boundary between Lithologies I and II (Figure 9a). It does not progress inward in slice 0484 (Figure 9a,b), but it does continue inward in slices below. Fracture B lies mainly in Lithology I (Figure 9a,c). Fractures C and D are visible in both the LH segmentation and the CT image (Figure 9a,b), positioned on either side of the vein, which is primarily segmented as Lithology IV. However, fractures C and D are though not continuous along the length of the vein. On the opposite side of the Lithology II-rich region along which Fractures C and D run, the alignment of Fractures E and F, along with the presence of the LL component between them (Figure 9a), suggests that they form a single fracture. This idea is confirmed by the CT image (Figure 9b), which shows a continuous fracture between E and F. The VV method segmented this fracture intermittently, a point discussed further in Nature of the Low LAC values (LL) Component Section.

Patches are predominantly found in the region dominated by Lithology I (Figure 9a,c, the red dashed box). In the CT image (Figure 9d), voxels associated with these patches appear brighter than those associated with Fracture B or with the surrounding void indicating they are filled with material denser than the air but lighter or, at least, compositionally distinct from the surrounding matrix. Further analyses are required to better understand the nature of the material responsible for the detection of these patches. No fractures or patches are found in the Lithology III-rich central region (Figure 9a).

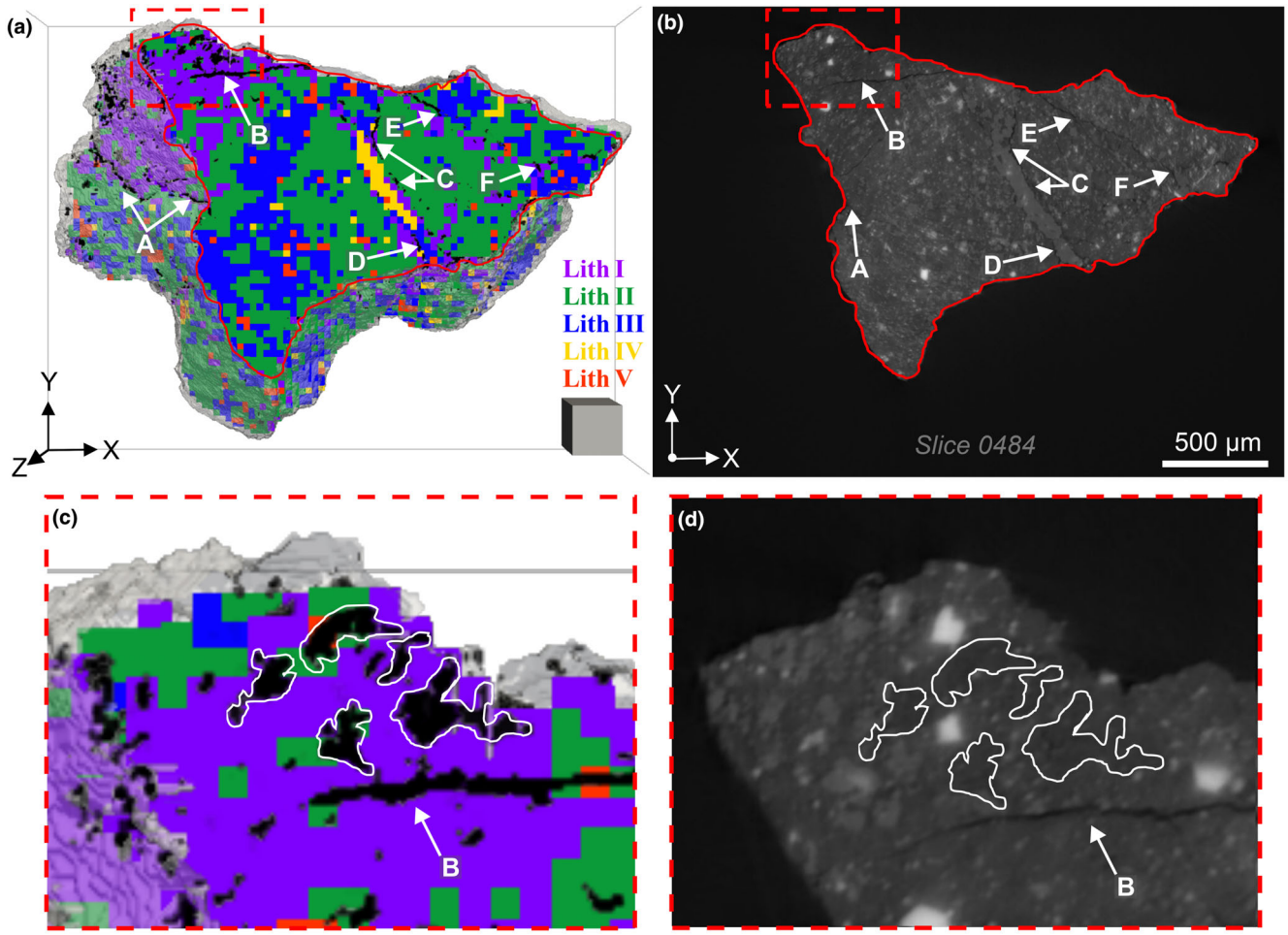

FIGURE 9. (a) Result of the Local Histogram segmentation on roughly half of the sample (20 first macroslices over the 48) overlapped with the results of low LAC value component in black (slices 0000 to 0484). Gray contours are for the sample shape while solid red contours represent the contours of the sample from the CT image of slice 0484 (b). The scale box size is 250 μm. In both panels, the white arrows indicate the fractures and the dashed red square indicates the region of dark patches, close-ups of which are shown in (c) and (d), with the dark patches surrounded by solid white outlines. Note that the volume of the LH segmentation and A0159 shape model are not in perfect agreement. This mismatch is mainly due to the enlargement or reduction of the two data sets to allow the 3D visualization using the open-source software Quasar.

Table 4 summarizes the specific 3D organization of lithologies and the particular affinities between the LL component (fractures and patches) and lithologies.

Mineralogical Description Using SEM Analysis

We present the results of the SEM analysis conducted on the Xe-pFIB sections that were selected based on the 3D distribution of lithologies. The objective was to characterize the mineralogical phases in A0159 to evaluate the accuracy of our newly developed LH method in detecting lithologies. Prior to SEM imaging, a detector collided with A0159, widening the central fracture on *Pangea*, indicated in the BSE images (Figure 10a). This damage was absent in the SR-μXCT data set, acquired earlier. However, the contours of the *Pangea* and Cut2 sections observed in SEM (Figure 10a–c) were correlated with the results of the LH segmentation performed on SR-μXCT data (Figure 10d) to aid comparison.

Matrix is the most abundant component in both sections (*Pangea* and Cut2), although it is compositionally heterogeneous. Figure 10c illustrates the chemical variability within the matrix by mapping the S/(Si + S) ratio, where the degree of sulfur enrichment increases from blue to yellow. The colored map was produced by analyzing the matrix separately—excluding coarser minerals such as sulfides, oxides, and Ca-rich phases (mainly carbonates)—and then overlaying the map with the Ca-rich detections. Therefore,

the remaining white phases in this map are representative of coarse sulfide and oxide minerals. In some regions, the elevated S/(Si + S) indicates sulfur enrichment within the matrix. A BSE image of a magnified region reveals that these sulfur-enriched areas contain a higher proportion of sub-micrometer sulfides intimately

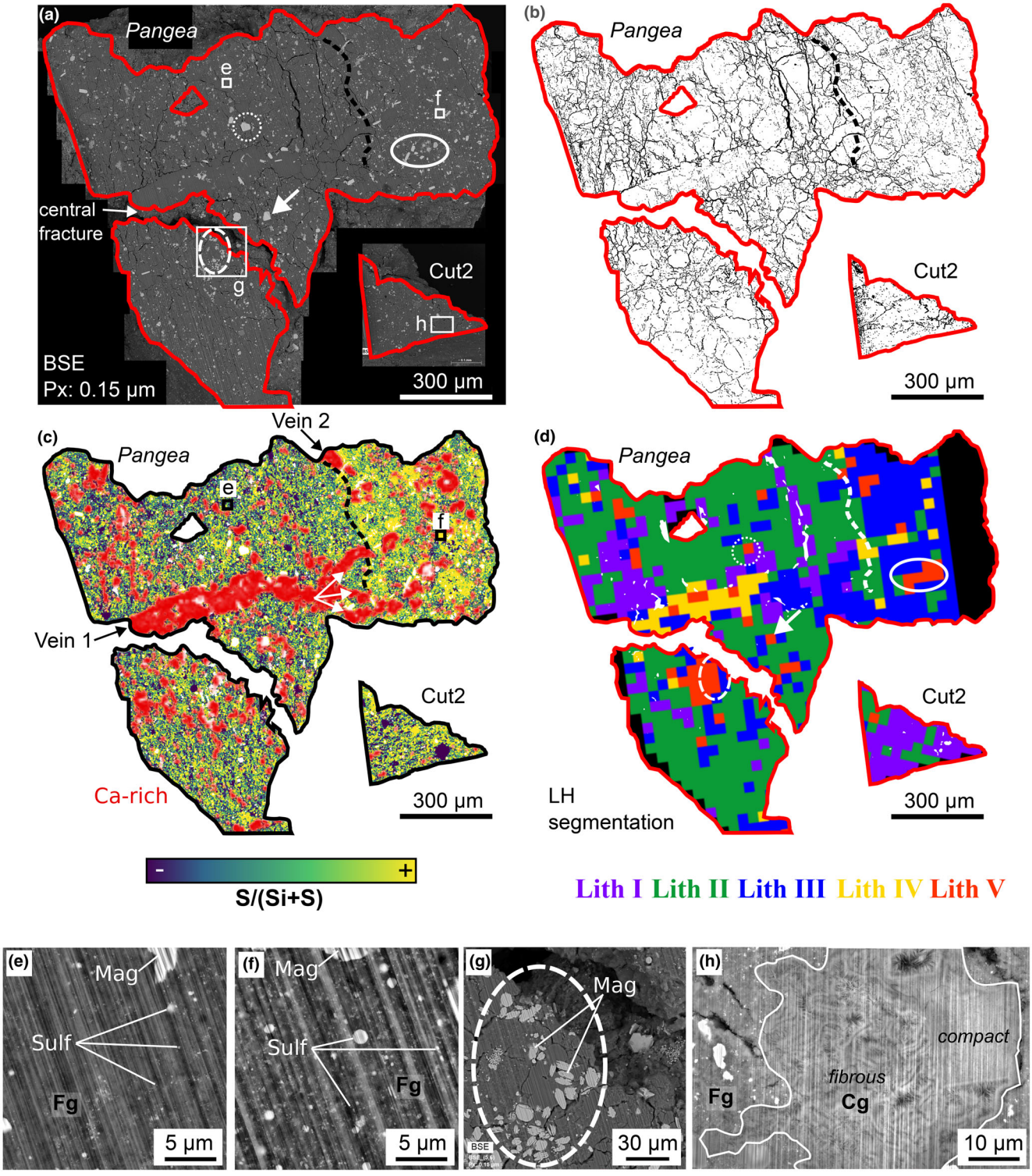

FIGURE 10. (a) Backscattered secondary electron (BSE) images of p-FIB sections *Pangea* and Cut2. (b) Extracted and enhanced low-density materials (pores, fractures, OM) using a grayscale threshold on BSE images of (a). (c) X-ray map from scanning electronic microscopy data showing the S/(S + Si) variation in the matrix, overlaid with the Ca-rich component in red. White phases are coarser opaque minerals. The white arrows indicate the direction of the main vein of carbonate (Vein1). (d) Local Histogram (LH) segmentation results of macroslices containing the CT image slices 0495 and 0840 corresponding to Xe-pFIB sections *Pangea* and Cut2. The LH results were superimposed by the low LAC values component extracted from the voxel-by-voxel segmentation, shown in white. (e) and (f) BSE close-ups of two fine-grained (Fg) phyllosilicates-rich regions, located in (a) and (c), sampling the dichotomy between the sub-micrometer sulfide-depleted matrix (e) and the enriched one (f) from both sides of the dashed line. (g, h) BSE close-ups of an aggregate rich in magnetite grains and a coarse-grained (Cg) phyllosilicate showing a fibrous and compact structures, respectively. (e–h) Mag, magnetite; Sulf, sulfide. Dotted, dashed, and solid circles in (a) and (g) indicate a large pyrrhotite mineral and two aggregates of opaques, respectively, and are correlated with the location of Lithology V macrovoxels in (d). The white arrow in (a) and (d) indicates a second large grain of pyrrhotite. Squares in (a) and (c) indicate (e–h) close-up locations. The dashed black (a–c) or white (d) line indicates the boundary between Lithologies II and III while red contours in (a–d) indicate the limit of *Pangea* and Cut2 sections from (a).

intermixed with the matrix (Figure 10f). Conversely, other regions appear more (or entirely) depleted in such sulfides (Figure 10c,e,h). A region exhibiting a total absence of sulfides is observed in the Cut2 section (blue region in Figure 10c); a BSE image of this round-shaped structure region is shown and outlined by a white solid line in Figure 10h. This structure measures roughly 50 × 50 μm and accounts for ≈5% of the Cut2 surface section. The structure is divided into two distinct parts: one exhibits a fibrous texture with a higher proportion of low-density material (likely pores) and is interpreted as a coarse-grained (Cg)-phyllosilicate (e.g., Aléon-Toppani et al., 2024; Leroux et al., 2023); the other appears more compact, homogeneous, and structureless with sharper boundaries. Neither part shows significant organic matter (OM) enrichment. Additional smaller Cg-phyllosilicates were observed in the *Pangea* and Cut2 sections. The matrix consists mostly of fine-grained (Fg) phyllosilicates containing sulfides (Figure 10e,f) and exhibiting a much less developed fibrous structure as indicated in Figure 10h.

Carbonates are seen in red in the colored map (Figure 10c), and we confirm them to be dolomite based on the 1:1 proportion of calcium (Ca) and magnesium (Mg). No breunnerite or calcite was detected. Figure 10c illustrates that dolomite varies in size and shape, with the main vein (Vein 1) extending ≈900 μm across *Pangea* and branching into three directions (indicated by solid white arrows). The vein width is irregular, ranging from 40 to 100 μm at its thickest section. A smaller vein (Vein 2, top of *Pangea*) is about 160 μm long and 20–70 μm wide. Other individual carbonate grains ranging from a few to several hundred microns in size are observed—some of which appear to align in chains. These carbonates are heterogeneously distributed across the sections, leading to carbonate-enriched (e.g., right side of the black dashed line in *Pangea*) and carbonate-depleted regions (e.g., Cut2). Both individual carbonate grains and veins occasionally enclose other mineral phases, such as a large (18 × 10 μm) P-rich grain attributed to a Ca-phosphate (close-up in Figure S4c), or opaque phases—either sulfides or oxides—represented in white in Figure 10c, or in yellow and blue, respectively, in Figure S4c.

Opaque phases, including sulfides and oxides, appear as the brightest features in BSE images (Figure 10a,e–h), consistent with their high attenuation in the SR-μXCT data set. These phases vary in distribution, size, and shape, as visible in both *Pangea* and Cut2 sections (Figure 10a) and close-ups (Figures 10e–g and S4a). As previously introduced, a clear dichotomy is observed in the *Pangea* section: one region shows an enrichment in sub-micrometer sulfides within the matrix (right of the black dashed line in Figure 10c; close-up in Figure 10f), while the other region is depleted in sulfides (left of the black dashed line in Figure 10c; close-up in Figure 10e). Sulfides in *Pangea* range in size from nanometers to a few tens of microns. The largest opaque observed in *Pangea* (dashed circle in Figure 10a) is a ≈30 μm sulfide, identified as a pyrrhotite. In contrast, magnetite minerals are generally smaller and exhibit a variety of morphologies (Figure S4a). Magnetite can also occur as aggregates intermixed with carbonate, matrix components, or both (dashed circle in Figure 10g).

Low-density materials, shown in Figure 10b, were extracted from the BSE images (Figure 10a) using a thresholding method and enhanced using ImageJ to improve visibility. Similar to the LL component from the VV segmentation, low-density materials resemble fractures. Some rectangular-shaped objects (Figure S4b) were identified and attributed to compounds enriched in OM and containing small opaque phases. No OM-filled fractures were found. Thus, most of the detected low-density materials account for empty fractures. There was a noticeable difference in abundance of fractures following the previously observed dichotomy between sub-micrometer sulfide-enriched and depleted regions. The sulfide-depleted region shows more and larger fractures (left of the black dotted line, Figure 10b)

compared to the sulfide-enriched region (right of the black dotted line, Figure 10b). Several fractures appear perpendicular to Vein 1, while others are aligned along its length (Figure 10b,c). In Cut2, only a few small fractures were detected, with most of them located near the Cg-phyllosilicate (Figure 10b).

SEM analysis confirms (i) the heterogeneous mineral distribution in A0159, (ii) the widespread presence of carbonates, and (iii) the occurrence of a millimeter-sized vein and individual grains of dolomite. It also reveals a matrix dichotomy, with a region rich in sub-micrometer-sized sulfides hosting a few fractures and a region depleted in sulfides with more and larger fractures. This spatial disparity aligns with the detection of distinct lithologies on either side of the white dashed line using our LH segmentation method (Figure 10d).

DISCUSSION

In this section, we address three main points: (i) the VV segmentation, beginning with the verification of the selected LAC values for each major component (matrix, carbonate, opaque, and low LAC values [LL]), followed by the interpretation of the nature of patches; (ii) the user-independent nature of the LH segmentation method versus the user-dependent VV method, emphasizing the advantages of the LH approach and its potential integration into a multi-analytical workflow for the analysis of extraterrestrial samples; and (iii) the initial results obtained from applying LH segmentation to Ryugu grain A0159.

Limitations of the VV Method and Nature of the LL Component

To verify the accuracy of the LAC selection, we conducted a complementary analysis using SEM and SR-μXCT data. SEM data provided a precise mineral phase identification and accurate localization on the *Pangea* and Cut2 sections, while SR-μXCT data enabled the measurement of their corresponding LAC values.

Matrix, Carbonate, Phosphate, and Opaque

Given the observed dichotomy for the matrix component (Figure 10a–d), we examined the LAC values of two matrix-rich regions, similar to areas in Figure 10e, f. The sub-micrometer sulfide-rich and sulfide-poor matrices show LAC ranges of [4.72–5.41] and [3.59–4.41], respectively. Our selected matrix interval of [3.5–5] closely encompasses both regions.

For the *carbonate* component, a region within Vein 1 yielded a measured LAC range of [5.2–6.2] closely matching our selected interval [5.5–6.5]. However, the measured interval of carbonate [5.2–6.2] overlaps with that of the sulfide-rich matrix [4.7–5.4], illustrating that similar LAC values can correspond to different components. This overlap complicates interval selection and can lead to false segmentation and misinterpretations. Given the proximity of the intermediate LAC ranges (carbonate [5.5–6.5] and sulfide-rich matrix [4.7–5.4]), it is likely that some voxels from the sub-micrometer sulfide-rich matrix were misclassified as carbonates and conversely. The 3D distribution of the diffuse carbonate-rich region resulting from the VV segmentation (bounded by white dashed lines in Figure 6) aligns with the 3D distribution of Lithology III identified by the LH segmentation method (Figure 8). Thus, on the *Pangea* section, this diffuse carbonate-rich region coincides with the region segmented as Lithology III to the right of the white dashed line (Figure 10d), as well as with the region whose matrix is enriched in sub-micrometer sulfides on the colored map (Figure 10c).

We identified a large (20 × 20 μm) *phosphate* grain on the lower part of the *Pangea* section. Its LAC values range [6.00–7.35], overlapping with the carbonate interval of [5.5–6.5]. This indicates that part of the carbonate modal abundance may correspond to phosphate.

For *opaque* phases, a framboidal magnetite aggregate and a large pyrrhotite grain were identified, with LAC intervals of [8.44–12.54] and [9.92–13.04], respectively. A threshold of LAC >9 was selected to define opaque phases, mostly encompassing both minerals. These analyses also confirm that sulfides and oxides cannot be distinguished using our SR-μXCT data set.

This analysis of LAC intervals (i) reveals that the minerals composing A0159 have very similar LAC values, and consequently, (ii) highlights the difficulty of precisely and consistently assigning a specific value range to a given component, and (iii) underscores the limitations to distinguish certain mineral phases through CT image analysis. Hence, despite its ability to estimate the modal proportion of mineral phases in the sample and to reveal their spatial distribution, the VV method remains limited. While it does enable the individual analysis of specific components such as the carbonate or LL components, it does not allow for the automated and independent detection of mineralogical assemblage.

Nature of the Low LAC Values (LL) Component

Organic Matter

As noted in previous studies, OM and pores are difficult to distinguish in SR-μXCT data due to their low density and low attenuation (Tsuchiyama et al., 2021); therefore, a proportion of the LL component from the VV method could be due to OM-rich compounds. In our study, the two OM-rich objects observed in SEM (Figure S4b) were not located in the SR-μXCT data, making the measure of their LAC impossible.

Furthermore, no particular OM enrichment was observed when comparing SEM data with the distribution of the LL component. Thus, the LL component detected does not appear to correspond to OM-rich compounds.

Fractures

Most of the features represented by the LL component (in black in Figure 9a,c) were attributed to fractures, consistent with the description of low-density material (detected using BSE images; Figure 10b). As we observed fractures of varying widths, we investigated the LAC intervals corresponding to larger (≈10 μm wide) and smaller (≈5 μm wide) fractures from the *Pangea* section. The larger fractures have LAC values in the range [0.9–3.5], while smaller fractures fall within [3.2–4.5]. We set an intermediate threshold below 3, favoring the detection of larger fractures. This result is consistent with (i) the estimated width of fractures derived from the description of the LL component (The 3D Low LAC Values (LL) Component Description and Distribution Within Lithologies Section) and (ii) the nonsegmentation of smaller fractures observed in the CT image of slice 0484 (Figure 9b). For instance, the thin fracture connecting the larger fractures E and F was not segmented (Figure 9a,b). Due to its variability in width, only the larger parts of the fracture were captured by segmentation, confirming the intermediate interval's enhanced sensitivity for detecting large-sized fractures. A notable discrepancy was observed between the abundance of fractures resulting from BSE image analysis (in black, Figure 10b) and the SR-μXCT segmentation (in white, Figure 10d) mainly due to the resolution differences. The BSE pixel size is 0.15 μm, and the SR-μXCT voxel size is 1.295 μm.

Patches

Less frequent than fractures, patches appear embedded with materials and are mainly located in Lithology I dominated regions. Combining both LH and VV results allows for the identification of small patches in the Cut2 section, which is mainly segmented as Lithology I (Figure 10d). At the location of these patches, SEM observations revealed the presence of a Cg-phyllosilicate surrounded by small fractures (Figure 10c,d). We suggest that these patches may represent Cg-phyllosilicates, small-scale fractures, or a combination of both. In summary, the modal abundance of the LL component in grain A0159 is primarily associated with large open fractures (≈10 μm) and, to a lesser extent, with patches that likely correspond to Cg-phyllosilicates, thin fractures (<2 μm), or both.

Capabilities and Potential of the LH Segmentation

Our study was motivated by the detection of distinct mineralogical assemblages that are often associated with the presence of clasts in breccia samples, such as those in Ryugu (Nakamura et al., 2023; Yamaguchi et al., 2023). The terms "breccia" and "clasts" typically imply that an impact event has occurred (Bischoff et al., 2006), resulting in the fracturing and re-accretion of fragmented material from different sources—either from separate parent bodies or from distinct locations within the same body. However, the coexistence of different mineralogical assemblages does not necessarily translate to an impact-related process. Hydrothermal alteration, for instance, can produce alteration fronts within a single and initially homogeneous lithology.

The experimental work of Suttle et al. (2022), aiming to reproduce the hydrothermal alteration on CM chondrite parent bodies, observed alteration fronts with the presence of a more altered matrix abutted against a less altered one. Here, the initial starting material was CO chondrite pellets, rich in anhydrous minerals and in which no clasts were reported. Additionally, recent analyses of Bennu samples, a B-type carbonaceous asteroid whose samples were returned by the OSIRIS-REx mission, revealed sulfide-enriched and sulfide-depleted lithologies in direct contact (Connolly Jr et al., 2025). This juxtaposition has been interpreted as a reaction front caused by sulfur remobilization within pre-existing phyllosilicates. These two examples illustrate that the presence of adjacent yet compositionally distinct lithologies can result from processes alternative to impact brecciation. In the following discussion section, we deliberately avoid interpreting the geological processes that may be responsible for distinct lithologies in sample A0159. However, it will be briefly addressed in A0159 3D Lithologies and Large Fractures Section and will be further discussed in detail in a subsequent publication.

An Independent and Adaptable Method to Detect and Analyze Lithologies in 3D

While the VV segmentation method requires user intervention for minerals selection and subsequently, the delineation of mineralogical assemblages, our LH segmentation method successfully identifies such heterogeneities through a semi-automatic and unsupervised approach. Figure 5 provides a direct visual comparison of the results obtained using the two segmentation methods (Figure 5e–l) alongside the original SR-μXCT data set (Figure 5a–d).

On the one hand, the VV segmentation (Figure 5e–h) enhances the readability of the heterogeneous distribution of LAC values more efficiently than the original SR-μXCT data set. By assigning specific LAC values to distinct components, it becomes easier to identify variations in the distribution of components. Based on this segmentation (Figure 5e–h), users can manually define regions corresponding to similar mineralogical assemblages, as is commonly done on

artificially produced 2D surfaces using analytical approaches such as BSE or SEM (e.g., Alfing et al., 2019; Connolly Jr et al., 2025; Nakamura et al., 2023; Patzek et al., 2018), spectroscopy (e.g., Brunetto et al., 2023; Schultz et al., 2025), or on 2D slices of XCT data sets (e.g., Dionnet et al., 2022; Friedrich et al., 2025; Kerraouch et al., 2021). In this way, lithologies can be manually delineated based on component abundance (i.e., matrix-rich, carbonate-rich, or opaque-enriched regions). However, this process is user-dependent and subject to interpretation, particularly in determining the precise boundaries of a distinct mineralogical assemblage.

The segmentation of lithologies (Lith. I to V) obtained using our LH method (Figure 5i–l) is generally consistent with the mineralogical heterogeneities visible in the VV-segmented images (Figure 5e–h), as an experienced user would manually identify them. However, the LH method also detects lithologies that a trained eye might not necessarily distinguish. For example, comparing Figure 5f,j shows that the LH method (Figure 5j) segmented the lower left region of A0159 into two distinct zones. At the grain's edge, Lithology I is dominant, followed further inward by lithologies II. In contrast, in the VV segmentation (Figure 5f), the same region appears largely homogeneous, dominated by the matrix component, without any clear variation in the distribution of major components. At this stage, it is difficult to visually discern the distinction identified by the LH method in this area. Two—possibly complementary—hypotheses could explain this: (i) a sampling bias between the analysis of a single 2D slice (Figure 5f) and that of a macroslice comprising 25 successive slices (Figure 5j); and (ii) the sensitivity of the LH method to parameters beyond the solely presence or absence of a component, such as mineral structure, porosity, or grain size—aspects we discuss further in the following section.

A Method Sensitive to Subtle Mineralogical Variations

By comparing SEM results (Figure 10c) with LH-detected lithologies (Figure 10d), we confirmed that distinct lithologies are indeed due to different mineralogical assemblages. Lithology II (to the left of the dashed line in Figure 10d) is enriched in matrix with carbonate grains (Figure 10c), whereas Lithology III (to the right of the dashed line in Figure 10d) exhibits an enrichment in sulfur resulting from a higher proportion of sub-micrometer sulfides (Figure 10c), although also Lithology III also contains the matrix and carbonate component. These sulfides, as shown in Figure 10f, are of micrometer size and are intimately associated with the matrix (Aléon-Toppani et al., 2024; Leroux et al., 2023; Nakamura et al., 2023; Tsuchiyama et al., 2024). SR-μXCT data have a voxel size of 1.295 μm, making the sulfides too small to be directly segmented using the VV method. However, the LH method successfully detected and localized these two lithologies, both of which are matrix-dominated but differ in their sub-micrometer sulfide content. This observation demonstrates the sensitivity of the LH segmentation method to indirectly detect features smaller than the voxel size itself.

A Method Sensitive to Physical Properties

Multiscaled structures

By overlaying the LH and VV segmentations (Figure 9a,c), two distinct types of macrovoxels associated with Lithology I can be identified. The first type includes macrovoxels overlapped by the LL component (i.e., fractures or patches), while the second type of macrovoxels shows no such overlap. The C7 histogram, characteristic of Lithology I, was previously described as showing a higher proportion of LL materials compared to other histograms (Figure 7c). Accordingly, all macrovoxels classified as Lithology I exhibit a greater content of the LL component. In the first group—macrovoxels overlapped by the LL component—the presence of fractures and patches clearly explains their enrichment in LL material, which in turn led to their classification as Lithology I. In the second group, however, the LL material cannot be attributed to such features. Nor can a greater content of LL material be explained by an enrichment in organic matter, as no such increase was observed in Cut2, which is predominantly segmented as Lithology I (Figure 10d). We therefore propose that the component responsible for shifting the histogram toward lower LAC values may be of a structural nature, undetectable by the VV method, contributing to reduce the density of the matrix, such as nanoporosity as discussed below in A0159 Modal Abundance Section. The LH segmentation is thus sensitive to different scale physical properties such as micrometric-wide fractures as well as finer structures.

Multiscaled Minerals

In contrast to Lithology III, which contains small opaque minerals, Lithology V corresponds to regions with magnetite aggregates or large sulfides associated with the matrix, the carbonate components, or both (circled by white lines in Figure 10a,d,g). Although both lithologies (III and V) have similar mineralogy, their histograms exhibit considerably different shapes (Figure 7c). We attribute this difference to the size of the components sampled in each lithology. In Lithology III, most sulfides are smaller than the voxel size (1.295 μm) and are intimately associated with the matrix (Figure 10f). This close association increases the attenuation coefficient of the matrix, resulting in voxels with intermediate LAC values that are higher than those of the pure matrix but lower than those of the pure opaque phases. These small sulfides are,

therefore, indirectly detected by the LH segmentation method. In contrast, Lithology V contains larger opaque phases that can reach several tens of micrometers and can yield voxels composed entirely of opaque material, making them directly detectable by our method. As a result, macrovoxels in regions characterized by Lithology V exhibit histograms enriched in high LAC values. The distinction between Lithologies III and V demonstrates that the LH method is sensitive to the size of the minerals sampled within each macrovoxel. However, not all opaque aggregates or isolated minerals observed in the BSE images (Figure 10a) correspond are segmented into Lithology V (Figure 10d). This discrepancy likely reflects both (i) a comparison bias between the BSE images and the LH segmentation results—since BSE images only represent the sample surface, while LH data correspond to 3D volumes—and (ii) the existence of a limit in the size, the relative proportion, or both, of opaques required for a macrovoxel to be classified as Lithology V. To illustrate, the aggregate of magnetite grains (Figure 10g) spatially correlated with the Lithology V-segmented macrovoxels (Figure 10d) contains grains ranging from 1.2 to 18 μm with an average size of 6.5 ± 3.5 μm (the uncertainty here represents the standard deviation over 100 measurements). However, numerous other magnetite grains (or opaque phases more generally) of similar size dispersed throughout the *Pangea* matrix are not segmented as Lithology V, suggesting that, in the case of aggregates, the number or abundance of grains plays a significant role in the detection of Lithology V. To estimate this abundance, we used ImageJ on the BSE image of *Pangea* to calculate the relative surface proportions of opaque minerals over areas of approximately 33 × 33 μm (i.e., equivalent to 25 × 25 voxels in the SR-μXCT data set). A grayscale threshold was applied to isolate and segment bright phases (i.e., opaques), allowing the measurement of their relative surface area. A total of 13 non-overlapping areas were analyzed across the two aggregates indicated by the solid and dashed circles in Figure 10a,d,g. Assuming that these 2D surfaces are representative of the 3D macrovoxels classified as Lithology V at the location of these aggregates (Figure 10d), then micrometer-sized opaque phases must occupy at least 29 ± 5% of the total macrovoxel volume to be segmented as Lithology V.

In the case of the pyrrhotite identified in Figure 10a, marked by the dotted white circle, its large size (≈27 × 28 μm) is likely the main driver for its segmentation as Lithology V. Another pyrrhotite grain of similar dimensions (≈25 × 28 μm) was observed in the BSE images and appears to correspond to the location of a macrovoxel segmented as Lithology V (white arrow in Figure 10a,d). Based on the volume estimates of opaque minerals in Lithology V macrovoxel results, it appears that an opaque mineral (in this case, pyrrhotite) occupying 29% of a macrovoxel's volume is sufficient for that macrovoxel to be classified as Lithology V. For a macrovoxel of size 33 × 33 × 33 μm, 29% of the volume corresponds to a cubic mineral of approximately 22 × 22 × 22 μm, consistent with the dimensions of the pyrrhotite grains observed. Therefore, we estimate that 22 × 22 × 22 μm (or a volume of 10,648 μm^3) represents the minimum size (or volume) an opaque phase must reach within a 33 × 33 × 33 μm macrovoxel for it to be classified as Lithology V. Grain size is, therefore, an important factor to consider when selecting macrovoxel size.

An Adaptable Method

The macrovoxel size is a user-defined parameter, which makes our method highly adaptable. Depending on the objectives of a given study, different macrovoxel sizes can be explored to optimize the detection of lithologies. An appropriate macrovoxel size depends on several interrelated parameters, including the grain size of the mineral phases, the size of the analyzed sample, and the scale of the heterogeneities or mineralogical assemblages the investigation aims to detect. For example, if the macrovoxels are too large (approaching the size of the sample, as in Uesugi et al., 2013), the resulting histograms tend to smooth internal heterogeneities and merge distinct lithologies. Conversely, macrovoxels that are too small (comparable to the size of individual minerals) may contain only a single phase, leading to monomineralic histograms with low compositional diversity, as observed in histograms C10 and C8 in this study. The flexibility to define the macrovoxel size means that our LH method can be adjusted based on the characteristics of a given sample.

In our study, which initially targeted mineralogical assemblages ranging from 10 to 500 μm (Nakamura et al., 2023), the chosen macrovoxel size of 33 μm proved to be appropriate for detecting distinct lithologies. However, specific cases—such as macrovoxels dominated by carbonates or large pyrrhotite grains—indicate that this size may sometimes be insufficient to fully capture a true assemblage. Although these specific detections allowed us to highlight particular structures, such as the carbonate vein, they may represent a critical threshold between detecting an assemblage and detecting a single mineral phase. Given the adaptability of our method, a multiscale analysis combining different macrovoxel sizes could help reveal the presence of sub-lithologies within broader mineralogical assemblages. Similarly, a complementary analysis of the heterogeneities detected in the "non-simplified" segmentation of A0159 (Figure 7a,b) could indicate the presence of finer scale mineralogical assemblages within broader ones (i.e., results after representative histogram grouping in Figure 7c,d).

Adaptability of our method may also be improved by implementing macrovoxel oversampling (i.e., regular macrovoxel overlap), which could compensate for the resolution loss introduced by the transformation of the original SR-μXCT data set (Figure 4I) into macroslices. However, this enhancement would lead to a significant increase in data volume, processing time, and computational load for handling histograms derived from the original SR-μXCT data sets, which are already large (e.g., ~17 GB for A0159). Some steps of the method outlined in Figure 4 rely on open-source software, like Quasar for representative histogram extraction, or Tomviz, which enables 3D visualization and provides one of the key strengths of our method. These software tools are not designed to handle data sets of this scale and may fail to complete some steps of the method outlined in Figure 4. To address this limitation, we are planning to develop and improve the LH method's data-processing procedures to handle large data sets more efficiently.

A Method Exploiting 3D Strengths

Unlike traditional studies based on a single 2D surface of a sample, the LH method enables the analysis of small 3D volumes and thereby captures the diversity of mineralogical assemblages in three dimensions. It also allows for the examination of an entire sample, overcoming the sample representation limitations of 2D approaches. Analyzing the whole sample allows estimation of the relative proportions of both major and minor mineralogical assemblages (Table 4), providing an initial framework for comparison with other studies (see A0159 3D Lithologies and Large Fractures Section for Ryugu). This approach also facilitates data visualization through 3D software, offering the opportunity to analyze lithologies independently or together, and to detect specific assemblages (e.g., Figures 5i–l, 8a,b, 9a, 10d). 3D analysis of distinct lithologies, thus, opens new perspectives for interpreting the formation and evolution of mineralogical assemblages and enables the development of a preliminary chronological scenario.

For instance, Lithology IV (primarily corresponding to the carbonate vein) is bordered on either side by Lithology II (Figure 5i–l), suggesting—based on the principle of inclusion relationships in relative chronology (Lyell, 1864)—that Lithology IV was emplaced after Lithology II. Furthermore, the 3D distribution of carbonates (Figure 6), combined with LH results from the *Pangea* section (Figure 10d) and complementary 2D analyses, suggests that the carbonate vein (Lithology IV) traverses the boundary between Lithologies II and III (Figure 10c,d). This indicates—based on the principle of cross-cutting relationships (Lyell, 1864)—that the formation of Lithology IV postdates the event responsible for the dichotomy between Lithologies II and III. In addition, the localized region enriched in Lithology I, located along the edge of the sample (Figures 8a,b and 9a,b), indicates that this portion of the grain experienced a distinct geological history compared to the areas containing Lithologies II and III. Its position on the edge of the sample makes it difficult to establish precise chronological relationships, but the absence of direct contact with Lithology III may suggest a potential sequence such as Lithology I, followed by II, and then III. Finally, Lithology V, which occurs predominantly within Lithology III (Figure 5j,l), may share a genetic relationship with it.

At this stage, the LH method does not allow for definitive conclusions regarding the geological processes that produced and affected these lithologies; rather, its primary objective is to detect and visualize mineralogical assemblages in order to aid interpretation. Additional analyses—mineralogical, petrological, and isotopic—are required to refine possible formation and evolution scenarios. Nevertheless, by enabling precise 3D localization of lithologies or features of particular interest, the LH method helps users make more informed decisions prior to performing further, often destructive, analyses. This transition from 2D to 3D analysis proved especially valuable in selecting pFIB sections, with highly convincing results.

Its Integration in a Multi-Analytical Sequence

Thanks to its semi-automated nature, the LH method can be integrated into multi-analytical workflows, such as the one described by Aléon-Toppani et al. (2021). The method requires only an XCT data set, and since XCT is nondestructive and noninvasive (Cody et al., 2024; Glavin et al., 2024), it has become a standard tool for analytical workflows for sample return missions (e.g., asteroids Itokawa, Ryugu, and Bennu; Tsuchiyama et al., 2011; Nakamura et al., 2023; Lauretta et al., 2024). Notably, Tsuchiyama et al. (2002) were among the first to propose XCT for the curation of meteorites, emphasizing its potential for the noninvasive characterization of fragile samples prior to any destructive handling.

In this work, the LH method was developed using XCT data acquired from a synchrotron source and calibrated at a single energy level (25 keV in this study). An alternative approach to acquiring XCT data is using laboratory-based instruments. In such cases, the sample is analyzed using a so-called polychromatic source that spans a broad spectrum of X-ray energies. However, energy–matter interactions vary depending on the material's composition, density, and the X-ray energy itself, resulting in additional artifacts in the CT images. These artifacts—such as beam hardening—mean that voxel values in CT images cannot be directly interpreted as linear attenuation coefficient (LAC) values and thus as physical properties of the material as is possible with data

sets obtained from monochromatic sources. A typical beam hardening artifact resulting from a polychromatic source is the reduction of CT values of a mineralogical assemblage located deeper within a sample compared to the same assemblage closer to the sample surface. Despite significant efforts to correct and reduce artifacts when analyzing heterogeneous geological samples (Ketcham & Hanna, 2014), some residual effects may still influence the XCT data set. This may affect the reliability of the mineralogical interpretation using the LH method. Caution is therefore advised when applying this method to data acquired from polychromatic sources. Nonetheless, the LH method shows promising potential, and further testing on polychromatic acquisitions could help expand its applicability.

Traditionally, the study of heterogeneities in mineralogical assemblages is conducted on 2D surfaces prepared by conventional destructive techniques, such as polishing or ablation (Nakamura et al., 2023; Noguchi et al., 2014; Yamaguchi et al., 2023). However, such methods are not feasible for large sample sets, especially when the samples are rare and fragile. Moreover, the number of available samples continues to grow, with 1100 and 4438 samples of at least 1 mm in size already collected from asteroids Ryugu and Bennu, respectively (Lauretta et al., 2024; Yada et al., 2022). Upcoming missions, such as the Mars Sample Return mission, which will retrieve samples collected by the Perseverance rover (McSween et al., 2025), and the Martian Moons Exploration (MMX) mission, targeting Phobos (Kuramoto et al., 2022), will further increase the quantity of extraterrestrial materials available for analysis. As we mentioned previously, the LH method is currently not optimized for large data sets. However, the initial results presented here are very promising. The LH method would offer an adaptable approach for detecting and comparing heterogeneities across large data sets, ensuring reproducibility and significantly reducing analysis time. Integrating the LH method into workflows for the study of subtle heterogeneities would be particularly beneficial for: (i) identifying the uniqueness or similarities of samples, (ii) assessing the distribution and abundance of lithologies, and (iii) guiding users in making more informed selections for subsequent, more destructive analyses, such as polished section preparation, as in Nakashima et al. (2023).

Application on an Extraterrestrial Sample, A0159

In this section, we discuss the results of the two methods on the extraterrestrial sample A0159 returned from asteroid Ryugu and highlight the scientific questions raised by these initial results, which will be addressed in a subsequent paper.

A0159 Modal Abundance

The *matrix* is the dominant component (46.6 vol%, Table 2) in sample A0159, which aligns with previous studies on Ryugu grains (Ito et al., 2022; Leroux et al., 2023; Nakamura et al., 2022; Tsuchiyama et al., 2024; Yamaguchi et al., 2023). Reported matrix abundances range from 56.5 to 92.9 vol% in Yamaguchi et al. (2023) and ≈60–90 vol% in Tsuchiyama et al. (2024).

Carbonates are the second most abundant component (22.7 vol%, Table 2) in A0159 yielding a matrix-to-carbonate ratio of 2. Such an enrichment in carbonate is rarely observed in previous work. Two samples, A0037 (Yamaguchi et al., 2023) and particle A0064-FO023 (Tsuchiyama et al., 2024), show comparable enrichment with a carbonate proportions of 21and 18 vol% and corresponding matrix abundances of 64 and 56 vol%, respectively. These values correspond to matrix-to-carbonate ratios of approximately 3. Due to their similarity in carbonate proportions, we focus on these two samples for comparative purposes.

Opaques represent the third major component in A0159 (1.6 vol%, Table 2) consistent with the 2 vol% reported in A0064-FO023 (Tsuchiyama et al., 2024) but less with the 6.7 vol% reported in A0037 (Yamaguchi et al., 2023). These yield a carbonate-to-opaque ratio of 9 for A0064-FO023 and 3 for A0037. In contrast, A0159 exhibits a carbonate-to-opaque ratio of approximately 14, suggesting either a significant enrichment in carbonates or depletion in opaques. This discrepancy is likely due in part to a difference in analytical techniques. Yamaguchi et al. (2023) used field-emission secondary electron microscopy (FE-SEM) on polished 2D planar sections of millimeter-sized samples, detecting submicron sulfides among the opaque component. Tsuchiyama et al. (2024) employed nano-XCT on particles with sizes ranging from 10 to 180 μm with a spatial resolution of 200 nm, allowing the detection of submicron phases. In our study, only opaque objects larger than a few micrometers were detected via the VV segmentation and included in modal abundance estimates. As a result, smaller opaque phases were likely missed by our analysis, leading to an underestimation of their abundance and an inflated carbonate-to-opaque ratio.

The *LL* component (<1 vol%, Table 2) in A0159 is primarily attributed to porosity. However, porosity in Ryugu samples occurs across multiple scales, and its estimation varies significantly depending on the technique. Even within a single sample, estimates can differ. Tsuchiyama et al. (2024) distinguished two types of porosity: porosity corresponding to pores and cracks and nanoporosity inferred from phyllosilicates density. In sample A0064-FO023, these were estimated at 23.3% and 45.9%, respectively, a nearly twofold difference. Our measured porosity is much lower, reflecting the spatial

resolution limit and suggesting undetected smaller scale porosity (Dionnet et al., 2022; Friedrich et al., 2025). This complicates direct comparisons with previous studies. However, it is possible that the LH method detected indirectly signs of nanoporosity. Specifically, the proportion of the LL component responsible for the segmentation of Lithology I macrovoxels, previously interpreted as structural in nature, may reflect an increased nanoporosity. While undetectable by the VV segmentation due to its small size, this porosity would nevertheless influence the matrix structure, density, and reduce its attenuation coefficient.

Based on this analysis, we conclude that VV segmentation, despite its reliance on user interpretation, provides an accessible method to highlight the uniqueness of sample A0159, especially its carbonate enrichment. In this work, modal abundances were preliminarily estimated by averaging over the entire sample without accounting for internal heterogeneity. Given the new insights from the LH segmentation and the identification of multiple lithologies within the *Pangea* section, we plan to conduct a more detailed study on the modal abundance specific to each lithology in future work.

A0159 Carbonates Diversity

SEM analysis confirmed the high carbonate content in A0159 (Figure 10b) and the identification of carbonate as dolomite. The scattered carbonates detected by the VV segmentation may correspond to individual grains observed in SEM analysis, consistent with previous reports of carbonates in Ryugu samples that typically range from a few tens to several hundreds of micrometers (Nakamura et al., 2022, 2023; Yamaguchi et al., 2023). Notably, this study presents the first observation of a millimeter-scale dolomite vein in Ryugu material. Prior studies reported numerous small dolomite grains ($CaMg(CO_3)_2$) and less frequent but larger breunnerite grains ($(Mg, Fe)CO_3$) (Hatakeda et al., 2023; Ito et al., 2022; Loizeau et al., 2023; Nakamura et al., 2022, 2023; Nakato et al., 2023; Yamaguchi et al., 2023). Dolomite grains measure around 100 μm (Loizeau et al., 2023; Nakamura et al., 2022; Nakato et al., 2023) and can reach up to 0.4 mm, as observed in grain A0037 (Yamaguchi et al., 2023), whereas breunnerite grains can reach several hundreds of micrometers (Ito et al., 2022; Loizeau et al., 2023; Yamaguchi et al., 2023), with the largest crystal reported at 940 × 450 × 262 μm in sample C0002 (Nakamura et al., 2023).

In A0159, the carbonate vein and some larger carbonate grains appear to be composed of adjacent crystals, though further research is needed to understand their formation. Concerning carbonate veins, Schultz et al. (2025) observed similar structure in the Aguas Zarcas CM meteorite at boundaries between distinct lithologies, suggesting formation after brecciation events. In contrast, the carbonate vein in A0159 seems to be embedded within a single lithology (Lithology II). In asteroid (101955) Bennu, carbonate veins appear to be more common and larger, reaching up to 1 m in size (Kaplan et al., 2020), suggesting that fluid flow within the parent body may have occurred over distances of several kilometers. More recently, the report of Na-rich carbonates and other salt minerals in Bennu's returned samples by McCoy et al. (2025) suggests that carbonate veins may have formed through the evaporation of brine-like fluids. A more detailed study of the vein in relation to the lithologies present in sample A0159 is necessary to elucidate the evolutionary history of these carbonate structures, particularly regarding their relationship to lithology, aqueous alteration, and brecciation processes.

A0159 3D Lithologies and Large Fractures

LH segmentation enabled the detection and 3D visualization of five distinct lithologies distributed throughout A0159, each exhibiting unique spatial relationships. However, at this stage, it remains difficult to determine whether the detected and analyzed lithologies in A0159 correspond to clasts resulting from impact-related processes or any other event. As discussed in the introduction of Capabilities and Potential of the LH Segmentation Section, adjacent lithologies can result from processes alternative to an impact event, such as aqueous alteration (e.g., Connolly Jr et al., 2025; Suttle et al., 2022), a process suggested to have impacted the Ryugu parent body (Yamaguchi et al., 2023). In this section, we provide an early exploration into the possible origin of each lithology in A0159, though further analyses will be necessary to draw firm conclusions regarding the origin of these lithologies.

Lithology I, notably depleted in carbonates, shows a strong association with large fractures (≈10 μm) and is enriched in the LL component, including patches and possibly a less dense matrix. Lithology I is predominantly surrounded by Lithology II and is only rarely adjacent to Lithology III. Lithologies II and III are comparatively enriched in carbonates. As suggested previously (A Method Exploiting 3D Strengths Section), the spatial distribution and composition of these lithologies suggest a potential sequence that could have been emplaced by a progressive aqueous alteration, with increasing alteration from Lithology I to Lithology III. However, the presence of a large fracture between Lithologies I and II also supports an alternative brecciation hypothesis, in which Lithology I experienced a distinct geological history and may have been mobilized during an impact-driven fragmentation event on Ryugu or its parent body. This scenario could explain the presence of a Lithology I clast in contact with the more altered Lithologies II and III. In this case, establishing a

relative chronology based on geological principles is challenging due to the main position of Lithology I within the sample (A Method Exploiting 3D Strengths Section).

Lithologies II and III both primarily consist of matrix and carbonate components but differ in the abundance of sub-micrometric sulfides and large fractures. Specifically, Lithology III exhibits a matrix with a higher proportion of sulfides and fewer fractures compared to Lithology II. These differences suggest variations in mechanical properties, a distinct geological history, or both, which may have led to increased fracturing in Lithology II. Interestingly, fractures in Lithology II are observed both parallel and perpendicular to the millimeter-scale carbonate vein, suggesting a possible genetic link between the vein and the fracture network. Regarding the dichotomy between Lithologies II and III, an impact-related event, an alteration front formation, or a combination of both are all conceivable scenarios, but current observations do not allow us to definitively exclude any of them.

Lithology IV, primarily associated with the vein and large carbonate grains, is mainly located within Lithology II. As suggested in A Method Exploiting 3D Strengths Section, the vein was likely emplaced after Lithology II (principle of inclusion), as well as after the event that brought Lithologies II and III into contact (principle of cross-cutting relationships), either chemical (e.g., locally different alteration) or physical (e.g., impact-related event).

Lithology V mainly corresponds to monomineralic assemblages or assemblages rich in opaque minerals. The 3D distribution reveals its heterogeneous presence within the sample, as well as its association with Lithologies II and III. This suggests that these host lithologies are more likely to contain larger mineral phases—particularly opaque minerals—compared to Lithology I. These occurrences may also point to a potential genetic relationship in their formation.

Mikouchi et al. (2022, 2025) used FE-EPMA and BSE imaging on polished sections of Ryugu to propose a lithological classification based on mineralogical assemblages and estimated the relative proportion of each lithology. The major lithology, accounting for ≈42% of the 50 analyzed polished sections, is an altered lithology rich in phyllosilicates and containing dolomite, magnetite, Fe-Ni sulfides, and Ca-phosphates. Both our lithologies II and III (45% and 35% in A0159, respectively, Table 4) are consistent with this major lithology in terms of mineralogy and abundance. However, the detection of two distinct lithologies (Lith. II and III), both with mineralogical compositions similar to the main lithology detected in Mikouchi et al. (2022, 2025), demonstrates not only (i) the effectiveness of the LH method in identifying major mineralogical assemblages but also (ii) its ability to discriminate lithologies with subtle differences—possibly pointing to subcategories within the main lithology. This suggests that the LH method can enhance the lithological characterization of Ryugu samples and offer new insights into their formation and evolutionary history. The second most abundant lithology identified by Mikouchi et al. (2022, 2025) (≈22%) is less altered, indicated by the presence of olivine, and the third (≈16%) is a lithology similar to their most abundant lithology but instead contains both dolomite and magnesite. In contrast, sample A0159 shows no evidence of anhydrous silicates such as olivine, and all observed carbonates were identified as dolomite. Less abundant lithologies were also discussed: one with an abundance of 11% depleted in small carbonates ($\approx < 1$ vol% and $\approx < 10$ μm in size) and another with an abundance of 6% containing large ($\approx > 100$ μm) carbonate aggregates (Mikouchi et al., 2022, 2025). These are consistent in both abundance and mineralogy, with Lithologies I (11%) and IV (5%) in sample A0159 (Table 4). Lithology V in A0159, which consists of aggregates of opaque minerals—particularly magnetite—was either not observed or not classified as a distinct lithology in the work conducted by Mikouchi et al. (2022, 2025). Moreover, the detection of lithologies not previously reported, the non-detection of certain ones (such as the least altered lithology or those containing magnesite), the high abundance of carbonates, and the presence of a millimetric dolomite vein all point to the specific nature of grain A0159. By extension, these findings also support the hypothesis of a complex geological evolution for asteroid Ryugu (Yamaguchi et al., 2023).

CONCLUSIONS

We developed a new SR-μXCT data processing method that enables the three-dimensional detection and analysis of lithologies in a Ryugu grain. This approach was combined with a conventional global grayscale threshold segmentation method, VV segmentation, which assigns each voxel to a specific component. The traditional VV method remains a simple and effective tool for visualizing the distribution of major mineral phases and global sample heterogeneities in a given sample. However, it relies heavily on user input to correctly identify mineral phases, select appropriate LAC intervals, and draw lithology boundaries.

The LH segmentation method developed herein is semi-automated and requires minimal user intervention. The LH method successfully identified lithologies with close mineralogical assemblages, later confirmed, and further characterized by complementary SEM analyses. The SEM analyses revealed that most lithologies were dominated by a matrix component, indicating that the LH method is

particularly well suited for relatively homogeneous samples. Additionally, the method demonstrated sensitivity to a range of structures, including fractures and mineral phases. For example, the LH method independently detected one lithology containing coarse-grained sulfides and another enriched in sub-micrometric sulfides within the matrix, despite these sub-micrometer features being smaller than the voxel size of the SR-μXCT data set. The LH method thus exhibits sensitivity in the detection of structures beyond the spatial resolution limit. Despite its sensitivity to multiple physicochemical parameters (such as mineralogy, structure, and porosity) occurring at small scales within the sample—sometimes even smaller than the voxel size—the LH method nevertheless reveals broader mineralogical assemblages, which can extend over several hundred micrometers and even reach the millimeter scale.

The LH method operates independently of other techniques (e.g., VV segmentation, SEM, FTIR) in the detection of mineralogical assemblages. Based on the work of Uesugi et al. (2013), the LH method could be developed to target more refined and accurate characterization of the mineralogical and compositional makeup of lithologies, using histogram analysis. Currently, the LH method still requires further analyses to identify the exact mineral assemblages it is capable of detecting. For this purpose, the threshold-based VV method remains easily implementable, especially in terms of computational time, and is highly complementary to the LH method. It enabled (i) an approximation of the mineralogical assemblage associated with histograms and identified lithologies, (ii) the identification of specific distributions of certain components, and (iii) when combined with LH, it highlighted the presence of large fractures in relation to specific lithologies. Together, these approaches offer a new framework for the analysis and interpretation of 3D data sets from brecciated samples, as well as those with diverse assemblages, thereby enhancing our understanding of their formation processes. Applied to the millimeter-sized Ryugu sample A0159, this combined approach revealed five distinct lithologies each associated with specific relationships with large (≈10 μm wide) fractures. We also identify, for the first time, a millimeter-scale dolomite vein in a Ryugu sample. These findings point to a complex geological history, raising key questions about the processes that shaped the observed heterogeneities, which we will address in future work.

Given its semi-automatic nature, the LH method can be applied to multiple samples in parallel. Initial tests on various Ryugu samples have yielded promising results: distinct assemblages were identified in several samples, while others appeared to be highly localized. However, further investigation is needed to interpret these findings fully. As previously mentioned, the current data processing stage of the LH method is limited by the large size of the data sets, which must be addressed in future developments. Once optimized, the LH method will enable large-scale comparative studies across samples and facilitate the detection of both unique and shared lithologies. Finally, the adaptability of the LH segmentation approach makes it promising for application to brecciated samples from other planetary bodies, such as lunar or Martian breccias (McSween et al., 2025; Shi et al., 2024), but more broadly to terrestrial or extraterrestrial rocks exhibiting heterogeneity in mineralogical assemblages.

Acknowledgments—Ryugu A0159 sample was generously provided by JAXA during the first AO of Hayabusa2 samples (project entitled "Evolution processes of Ryugu, from aqueous alteration to space weathering"). We are thankful to Megumi Matsumoto for helping with the procedures to realize Xe-pFIB sections and Eric Quirico for providing Orgueil samples used in the development of Xe-pFIB sectioning; Sylvain Pont for the MEB acquisition; Ferenc Borondics and Christophe Sandt for helping with the Quasar software and the FTIR measurements; Jean-Pierre Bibring, François Poulet, and Cédric Pilorget for enabling the use of MicrOmega instrument on the PTAL bench; François Brisset, Claire Boukari, and Jerôme Aléon for helping with sample preparation. We extend our grateful thanks to Corentin Le Guillou, Donia Baklouti, Zahia Djouadi, Cateline Lantz, Obadias Mivumbi, and the LARCAS team for their useful help and discussion. We are grateful to Scott Eckley and an anonymous reviewer for constructive and insightful suggestions on an earlier version of this manuscript. Results of this research have been obtained through the cooperation between IAS, CNRS, Université Paris-Saclay, and JAXA. This research was funded by the Centre National d'Etudes Spatiales (CNES, France, Hayabusa2 mission) and by the ANR project LARCAS under grant ANR-22-CE49-0009-01 of the French Agence Nationale de la Recherche. The FTIR measurements were supported by grants from Region Ile-de-France (DIM-ACAV) and SOLEIL.

Data Availability Statement—Due to the large size of the SR-μXCT data set (~17 GB), the data supporting the findings of this study are available from the corresponding author upon reasonable request. The code to reproduce this analysis is publicly available at https://github.com/LenaJosse/LH_meth. The matrix-rich, carbonate-rich, and the average FTIR spectra of A0159 shown in Figure 3 are available on the SSHADE infrastructure at doi: EXPERIMENT_ZeD_20250905_01.

Editorial Handling—Dr. Scott Sandford

REFERENCES

Aléon-Toppani, A., Brunetto, R., Aléon, J., Dionnet, Z., Rubino, S., Levy, D., Troadec, D., Brisset, F., Borondics, F., and King, A. 2021. A Preparation Sequence for Multi-Analysis of μm-Sized Extraterrestrial and Geological Samples. *Meteoritics & Planetary Science* 56: 1151–72.

Aléon-Toppani, A., Brunetto, R., Dionnet, Z., Rubino, S., Baklouti, D., Brisset, F., Vallet, M., et al. 2024. Correlated IR-SEM-TEM Studies of Three Different Grains from Ryugu: From the Initial Material to Post-Accretional Processes. *Geochimica et Cosmochimica Acta* 371: 1–30.

Alfing, J., Patzek, M., and Bischoff, A. 2019. Modal Abundances of Coarse-Grained (< 5 μm) Components within CI-Chondrites and Their Individual Clasts–Mixing of Various Lithologies on the CI Parent Body(Ies). *Geochemistry* 79: 125532.

Beck, P., Garenne, A., Quirico, E., Bonal, L., Montes-Hernandez, G., Moynier, F., and Schmitt, B. 2014. Transmission Infrared Spectra (2–25μm) of Carbonaceous Chondrites (CI, CM, CV-CK, CR, C2 Ungrouped): Mineralogy, Water, and Asteroidal Processes. *Icarus* 229: 263–277.

Beck, P., Quirico, E., Montes-Hernandez, G., Bonal, L., Bollard, J., Orthous-Daunay, F.-R., Howard, K., et al. 2010. Hydrous Mineralogy of CM and CI Chondrites from Infrared Spectroscopy and their Relationship with Low Albedo Asteroids. *Geochimica et Cosmochimica Acta* 74: 4881–92.

Berger, M., Hubbell, J., Seltzer, S., Chang, J., Coursey, J., Sukumar, R., Zucker, D., and Olsen, K. 2010. *Xcom: Photon Cross Section Database (Version 1.5)*. Gaithersburg, MD: National Institute of Standards and Technology. https://physics.nist.gov/xcom.

Bischoff, A., Scott, E. R., Metzler, K., and Goodrich, C. A. 2006. Nature and Origins of Meteoritic Breccias. In *Meteorites and the Early Solar System II*. Tucson: University of Arizona Press. 679–712.

Bishop, J., King, S., Lane, M., Brown, A., Lafuente, B., Hiroi, T., Roberts, R., Swayze, G., Lin, J.-F., and Sánchez Román, M. 2021. Spectral Properties of Anhydrous Carbonates and Nitrates. *Earth and Space Science* 8: e2021EA001844.

Bonse, U., and Busch, F. 1996. X-Ray Computed Microtomography (μCT) Using Synchrotron Radiation (SR). *Progress in Biophysics and Molecular Biology* 65: 133–169.

Bottke, W. F., Jr., Durda, D. D., Nesvorný, D., Jedicke, R., Morbidelli, A., Vokrouhlický, D., and Levison, H. 2005. The Fossilized Size Distribution of the Main Asteroid Belt. *Icarus* 175: 111–140.

Brunetto, R., Lantz, C., Fukuda, Y., Aléon-Toppani, A., Nakamura, T., Dionnet, Z., Baklouti, D., et al. 2023. Ryugu's Anhydrous Ingredients and their Spectral Link to Primitive Dust from the Outer Solar System. *The Astrophysical Journal Letters* 951: L33.

Cody, G. D., Alexander, C. M. O., Foustoukos, D. I., Busemann, H., Eckley, S., Burton, A. S., Berger, E. L., et al. 2024. The Nature of Insoluble Organic Matter in Sutter's Mill and Murchison Carbonaceous Chondrites: Testing the Effect of X-Ray Computed Tomography and Exploring Parent Body Organic Molecular Evolution. *Meteoritics & Planetary Science* 59: 3–22.

Connolly, H. C., Jr., Lauretta, D. S., McCoy, T. J., Russell, S. S., Haenecour, P., Polit, A., Barnes, J. J., Zega, T. J., et al. 2025. An Overview of the Petrography and Petrology of Particles from Aggregate Sample from Asteroid Bennu. *Meteoritics & Planetary Science* 60: 979–996.

Dionnet, Z., Aléon-Toppani, A., Brunetto, R., Rubino, S., Suttle, M. D., Lantz, C., Avdellidou, C., et al. 2022. Multiscale Correlated Analysis of the Aguas Zarcas CM Chondrite. *Meteoritics & Planetary Science* 57: 965–988.

Dionnet, Z., Rubino, S., Aléon-Toppani, A., Brunetto, R., Tsuchiyama, A., Lantz, C., Djouadi, Z., Baklouti, D., et al. 2024. Three-Dimensional Multiscale Assembly of Phyllosilicates, Organics, and Carbonates in Small Ryugu Fragments. *Meteoritics & Planetary Science* 59: 1859–76.

Ebel, D. S., and Rivers, M. L. 2007. Meteorite 3-D Synchrotron Microtomography: Methods and Applications. *Meteoritics & Planetary Science* 42: 1627–46.

Friedrich, J. M. 2008. Quantitative Methods for Three-Dimensional Comparison and Petrographic Description of Chondrites. *Computers and Geosciences* 34: 1926–35.

Friedrich, J. M., Chen, M. M., Giordano, S. A., Matalka, O. K., Strasser, J. W., Tamucci, K. A., Rivers, M. L., and Ebel, D. S. 2022. Size-Frequency Distributions and Physical Properties of Chondrules from X-Ray Computed Microtomography and Digital Data Extraction. *Microscopy Research and Technique* 85: 1814–24.

Friedrich, J. M., Riveros, E. M., Macke, R. J., Jaret, S. J., Rivers, M. L., and Ebel, D. S. 2025. Physical Properties, Internal Structure, and the Three-Dimensional Petrography of CI Chondrites. *Meteoritics & Planetary Science* 60: 632–645.

Friedrich, J. M., and Rivers, M. L. 2013. Three-Dimensional Imaging of Ordinary Chondrite Microporosity at 2.6μm Resolution. *Geochimica et Cosmochimica Acta* 116: 63–70.

Friedrich, J. M., Ruzicka, A., Macke, R. J., Thostenson, J. O., Rudolph, R. A., Rivers, M. L., and Ebel, D. S. 2017. Relationships among Physical Properties as Indicators of High Temperature Deformation or Post-Shock Thermal Annealing in Ordinary Chondrites. *Geochimica et Cosmochimica Acta* 203: 157–174.

Friedrich, J. M., Weisberg, M. K., and Rivers, M. L. 2014. Multiple Impact Events Recorded in the NWA 7298 h Chondrite Breccia and the Dynamical Evolution of an Ordinary Chondrite Asteroid. *Earth and Planetary Science Letters* 394: 13–19.

Glavin, D. P., Eckley, S. A., Aponte, J. C., Berger, E. L., Burton, A. S., Dworkin, J. P., Elsila, J. E., et al. 2024. Investigating the Impact of X-Ray Computed Tomography Imaging on Soluble Organic Matter in the Murchison Meteorite: Implications for Bennu Sample Analyses. *Meteoritics & Planetary Science* 59: 105–133.

Griffin, L. D., Elangovan, P., Mundell, A., and Hezel, D. C. 2012. Improved Segmentation of Meteorite Micro-CT Images Using Local Histograms. *Computers and Geosciences* 39: 129–134.

Hanna, R. D., and Ketcham, R. A. 2017. X-Ray Computed Tomography of Planetary Materials: A Primer and Review of Recent Studies. *Chemie der Erde* 77: 547–572.

Hanna, R. D., Ketcham, R. A., Edey, D. R., and O'Connell, J. 2022. 3D Porosity Structure of the Earliest Solar System Material. *Scientific Reports* 12: 8369.

Hatakeda, K., Yada, T., Abe, M., Okada, T., Nakato, A., Yogata, K., Miyazaki, A., et al. 2023. Homogeneity and Heterogeneity in near-Infrared FTIR Spectra of Ryugu Returned Samples. *Earth, Planets and Space* 75: 46.

Ito, M., Tomioka, N., Uesugi, M., Yamaguchi, A., Shirai, N., Ohigashi, T., Liu, M.-C., Greenwood, R. C., et al. 2022. A Pristine Record of Outer Solar System Materials from Asteroid Ryugu's Returned Sample. *Nature Astronomy* 6: 1163–71.

Jerram, D. A., and Higgins, M. D. 2007. 3D Analysis of Rock Textures: Quantifying Igneous Microstructures. *Elements* 3: 239–245.

Kaplan, H., Lauretta, D., Simon, A., Hamilton, V., DellaGiustina, D., Golish, D., Reuter, D., Bennett, C., et al. 2020. Bright Carbonate Veins on Asteroid (101955) Bennu: Implications for Aqueous Alteration History. *Science* 370: eabc3557.

Kawasaki, N., Nagashima, K., Sakamoto, N., Matsumoto, T., Bajo, K.-I., Wada, S., Igami, Y., et al. 2022. Oxygen Isotopes of Anhydrous Primary Minerals Show Kinship between Asteroid Ryugu and Comet 81P/Wild2. *Science Advances* 8: eade2067.

Kerraouch, I., Bischoff, A., Zolensky, M. E., Pack, A., Patzek, M., Hanna, R. D., Fries, M. D., et al. 2021. The Polymict Carbonaceous Breccia Aguas Zarcas: A Potential Analog to Samples Being Returned by the OSIRIS-REx and Hayabusa2 Missions. *Meteoritics & Planetary Science* 56: 277–310.

Ketcham, R., and Mote, A. 2019. Accurate Measurement of Small Features in X-Ray CT Data Volumes, Demonstrated Using Gold Grains. *Journal of Geophysical Research—Solid Earth* 124: 3508–29.

Ketcham, R. A. 2006. Accurate Three-dimensional Measurements of Features in Geological Materials from X-ray Computed Tomography Data. In *Advances in X-ray Tomography for Geomaterials*, John Wiley & Sons, Ltd. 143–48.https://doi.org/10.1002/9780470612187.ch9

Ketcham, R. A., and Hanna, R. D. 2014. Beam Hardening Correction for X-Ray Computed Tomography of Heterogeneous Natural Materials. *Computers & Geosciences* 67: 49–61.

King, A., Guignot, N., Zerbino, P., Boulard, E., Desjardins, K., Bordessoule, M., Leclerq, N., et al. 2016. Tomography and Imaging at the PSICHE Beam Line of the Soleil Synchrotron. *Review of Scientific Instruments* 87: 93704.

Kuramoto, K., Kawakatsu, Y., Fujimoto, M., Araya, A., Barucci, M. A., Genda, H., Hirata, N., Ikeda, H., et al. 2022. Martian Moons Exploration MMX: Sample Return Mission to Phobos Elucidating Formation Processes of Habitable Planets. *Earth, Planets and Space* 74: 12.

Kyle, J. R., and Ketcham, R. A. 2015. Application of High Resolution X-Ray Computed Tomography to Mineral Deposit Origin, Evaluation, and Processing. *Ore Geology Reviews* 65: 821–839.

Lauretta, D. S., Connolly, H. C., Jr., Aebersold, J. E., Alexander, C. M. O., Ballouz, R.-L., Barnes, J. J., Bates, H. C., Bennett, C. A., et al. 2024. Asteroid (101955) Bennu in the Laboratory: Properties of the Sample Collected by OSIRIS-REx. *Meteoritics & Planetary Science* 59: 2453–86.

Le Pivert-Jolivet, T., Brunetto, R., Pilorget, C., Baklouti, D., Bibring, J.-P., Carter, J., Hamm, V., et al. 2025. Water in Ryugu as a Property of Processes in its Parent Body. *Astronomy & Astrophysics* 695: A168.

Leroux, H., Le Guillou, C., Marinova, M., Laforet, S., Viennet, J.-C., Mouloud, B.-E., Teurtrie, A., de la Peña, F., Jacob, D., et al. 2023. Phyllosilicates with Embedded Fe-Based Nanophases in Ryugu and Orgueil. *Meteoritics & Planetary Science* 59:1947–65.

Lindgren, P., Hanna, R. D., Dobson, K. J., Tomkinson, T., and Lee, M. R. 2015. The Paradox between Low Shock-Stage and Evidence for Compaction in CM Carbonaceous Chondrites Explained by Multiple Low-Intensity Impacts. *Geochimica et Cosmochimica Acta* 148: 159–178.

Liu, M.-C., McCain, K. A., Matsuda, N., Yamaguchi, A., Kimura, M., Tomioka, N., Ito, M., et al. 2022. Incorporation of ^{16}O-Rich Anhydrous Silicates in the Protolith of Highly Hydrated Asteroid Ryugu. *Nature Astronomy* 6: 1172–77.

Loizeau, D., Lequertier, G., Poulet, F., Hamm, V., Pilorget, C., Meslier-Lourit, L., Lantz, C., Werner, S. C., Rull, F., and Bibring, J.-P. 2020. Planetary Terrestrial Analogues Library Project: 2. Building a Laboratory Facility for Micromega Characterization. *Planetary and Space Science* 193: 105087.

Loizeau, D., Pilorget, C., Riu, L., Brunetto, R., Bibring, J.-P., Nakato, A., Aléon-Toppani, A., Hatakeda, K., et al. 2023. Constraints on Solar System Early Evolution by Micromega Analysis of Ryugu Carbonates. *Nature Astronomy* 7: 391–97.

Lyell, C. 1864. *Principles of Geology: Or the Modern Changes of the Earth and its Inhabitants Considered as Illustrative of Geology*. New York: D. Appleton & Company.

McCoy, T. J., Russell, S. S., Zega, T., Thomas-Keprta, K., Singerling, S., Brenker, F., Timms, N., Rickard, W., et al. 2025. An Evaporite Sequence from Ancient Brine Recorded in Bennu Samples. *Nature* 637: 1072–77.

McSween, H. Y., Jr., Hamilton, V. E., and Farley, K. A. 2025. Perspectives on Mars Sample Return: A Critical Resource for Planetary Science and Exploration. *Proceedings of the National Academy of Sciences of the United States of America* 122: e2404248121.

Mikouchi, T., Masuda, M., Yoshida, H., Zolensky, M. E., and Nakamura, T. 2025. Lithology Comparison between Ryugu Samples and CI Chondrites: An Update. *LPI Contributions* 3088: 5211.

Mikouchi, T., Yoshida, H., Nakamura, T., Matsumoto, M., Tsuchiyama, A., Matsuno, J., Tsutsui, K., Zolensky, M. E., et al. 2022. Lithological Variation of Asteroid Ryugu Samples Returned by the Hayabusa2 Spacecraft: Assessment from the 18 Particles Distributed to the Initial Analysis "Stone" Team Hayabusa Symposium 2022.

Mirone, A., Brun, E., Gouillart, E., Tafforeau, P., and Kieffer, J. 2014. The PyHST2 Hybrid Distributed Code for High Speed Tomographic Reconstruction with Iterative Reconstruction and a Priori Knowledge Capabilities. *Nuclear Instruments and Methods in Physics Research Section B: Beam Interactions with Materials and Atoms* 324: 41–48.

Miyazaki, A., Yada, T., Yogata, K., Hatakeda, K., Nakato, A., Nishimura, M., Nagashima, K., et al. 2023. A Newly Revised Estimation of Bulk Densities and Examination of the Shape of Individual Ryugu Grains. *Earth, Planets and Space* 75: 171.

Nakamura, E., Kobayashi, K., Tanaka, R., Kunihiro, T., Kitagawa, H., Potiszil, C., Ota, T., et al. 2022. On the

Origin and Evolution of the Asteroid Ryugu: A Comprehensive Geochemical Perspective. *Proceedings of the Japan Academy, Series B* 98: 227–282.
Nakamura, T., Matsumoto, M., Amano, K., Enokido, Y., Zolensky, M. E., Genda, H., Tanaka, S., Zolotov, M. Y., et al. 2023. Formation and Evolution of Carbonaceous Asteroid Ryugu: Direct Evidence from Returned Samples. *Science* 379: eabn8671.
Nakashima, D., Fujioka, Y., Katayama, K., Morita, T., Kikuiri, M., Amano, K., Kagawa, E., and Nakamura, T. 2023. Development of Preparation Methods of Polished Sections of Returned Samples from Asteroid Ryugu by the Hayabusa2 Spacecraft. *Meteoritics & Planetary Science* 59: 1829–44.
Nakato, A., Yada, T., Nishimura, M., Yogata, K., Miyazaki, A., Nagashima, K., Hatakeda, K., Kumagai, K., et al. 2023. Variations of the Surface Characteristics of Ryugu Returned Samples. *Earth, Planets and Space* 75: 45.
Noguchi, T., Bridges, J. C., Hicks, L. J., Gurman, S. J., Kimura, M., Hashimoto, T., Konno, M., et al. 2014. Mineralogy of Four Itokawa Particles Collected from the First Touchdown Site. *Earth, Planets and Space* 66: 1–10.
Noguchi, T., Matsumoto, T., Miyake, A., Igami, Y., Haruta, M., Saito, H., Hata, S., Seto, Y., et al. 2023. Mineralogy and Petrology of Fine-Grained Samples Recovered from the Asteroid (162173) Ryugu. *Meteoritics & Planetary Science* 59: 1877–1906.
O'Brien, D. P., and Greenberg, R. 2005. The Collisional and Dynamical Evolution of the Main-Belt and NEA Size Distributions. *Icarus* 178: 179–212.
Patzek, M., Bischoff, A., Visser, R., and John, T. 2018. Mineralogy of Volatile-Rich Clasts in Brecciated Meteorites. *Meteoritics & Planetary Science* 53: 2519–40.
Pilorget, C., Okada, T., Hamm, V., Brunetto, R., Yada, T., Loizeau, D., Riu, L., et al. 2022. First Compositional Analysis of Ryugu Samples by the MicrOmega Hyperspectral Microscope. *Nature Astronomy* 6: 221–25.
Schneider, C. A., Rasband, W. S., and Eliceiri, K. W. 2012. Nih Image to ImageJ: 25 Years of Image Analysis. *Nature Methods* 9: 671–75.
Schultz, C., Milliken, R. E., Boesenberg, J., and Kerraouch, I. 2025. Near-and Mid-Infrared Spectral Diversity in the Aguas Zarcas Carbonaceous Chondrite and Implications for Inferring Aqueous Processes on Primitive Asteroids Using Remote Sensing. *Meteoritics & Planetary Science* 60: 876–915.
Schwartz, J., Harris, C., Pietryga, J., Zheng, H., Kumar, P., Visheratina, A., Kotov, N. A., et al. 2022. Real-Time 3D Analysis during Electron Tomography Using Tomviz. *Nature Communications* 13: 4458.
Shi, Y., Peng, W., Joy, K. H., Yu, X., Guan, Y., Bao, Z., Che, X., et al. 2024. Petrological, Chemical, and Chronological Study of Breccias in the Chang'e-5 Soil. *Meteoritics & Planetary Science* 59: 2296–2320.
Suttle, M., King, A., Ramkissoon, N., Bonato, E., Franchi, I., Malley, J., Schofield, P., Najorka, J., Salge, T., and Russell, S. 2022. Alteration Conditions on the CM and CV Parent Bodies–Insights from Hydrothermal Experiments with the CO Chondrite Kainsaz. *Geochimica et Cosmochimica Acta* 318: 83–111.
Toplak, M., Birarda, G., Read, S., Sandt, C., Rosendahl, S., Vaccari, L., Demšar, J., and Borondics, F. 2017. Infrared Orange: Connecting Hyperspectral Data with Machine Learning. *Synchrotron Radiation News* 30: 40–45.
Toplak, M., Read, S. T., Sandt, C., and Borondics, F. 2021. Quasar: Easy Machine Learning for Biospectroscopy. *Cells* 10: 2300.
Tsuchiyama, A., Matsumoto, M., Matsuno, J., Yasutake, M., Nakamura, T., Noguchi, T., Miyake, A., Uesugi, K., et al. 2024. Three-Dimensional Textures of Ryugu Samples and their Implications for the Evolution of Aqueous Alteration in the Ryugu Parent Body. *Geochimica et Cosmochimica Acta* 375: 146–172.
Tsuchiyama, A., Miyake, A., Okuzumi, S., Kitayama, A., Kawano, J., Uesugi, K., Takeuchi, A., Nakano, T., and Zolensky, M. 2021. Discovery of Primitive CO_2-Bearing Fluid in an Aqueously Altered Carbonaceous Chondrite. *Science Advances* 7: eabg9707.
Tsuchiyama, A., Nakamura, T., Nakano, T., and Nakamura, N. 2002. Three-Dimensional Description of the Kobe Meteorite by Micro X-Ray CT Method: Possibility of Three-Dimensional Curation of Meteorite Samples. *Geochemical Journal* 36: 369–390.
Tsuchiyama, A., Uesugi, K., Nakano, T., and Ikeda, S. 2005. Quantitative Evaluation of Attenuation Contrast of X-Ray Computed Tomography Images Using Monochromatized Beams. *American Mineralogist* 90: 132–142.
Tsuchiyama, A., Uesugi, M., Matsushima, T., Michikami, T., Kadono, T., Nakamura, T., Uesugi, K., Nakano, T., et al. 2011. Three-Dimensional Structure of Hayabusa Samples: Origin and Evolution of Itokawa Regolith. *Science* 333: 1125–28.
Uesugi, M., Uesugi, K., Takeuchi, A., Suzuki, Y., Hoshino, M., and Tsuchiyama, A. 2013. Three-Dimensional Observation of Carbonaceous Chondrites by Synchrotron Radiation X-Ray CT–Quantitative Analysis and Developments for the Future Sample Return Missions. *Geochimica et Cosmochimica Acta* 116: 17–32.
Watanabe, S., Hirabayashi, M., Hirata, N., Hirata, N., Noguchi, R., Shimaki, Y., Ikeda, H., Tatsumi, E., et al. 2019. Hayabusa2 Arrives at the Carbonaceous Asteroid 162173 Ryugu—A Spinning Top-Shaped Rubble Pile. *Science* 364: 268–272.
Yada, T., Abe, M., Okada, T., Nakato, A., Yogata, K., Miyazaki, A., Hatakeda, K., et al. 2022. Preliminary Analysis of the Hayabusa2 Samples Returned from c-Type Asteroid Ryugu. *Nature Astronomy* 6: 214–220.
Yamaguchi, A., Tomioka, N., Ito, M., Shirai, N., Kimura, M., Greenwood, R., Liu, M.-C., McCain, K., et al. 2023. Insight into Multi-Step Geological Evolution of c-Type Asteroids from Ryugu Particles. *Nature Astronomy* 7: 1–8.
Yokoyama, T., Nagashima, K., Nakai, I., Young, E. D., Abe, Y., Aléon, J., Alexander, C. M. O., et al. 2022. Samples Returned from the Asteroid Ryugu Are Similar to Ivuna-Type Carbonaceous Meteorites. *Science* 379: eabn7850.

SUPPORTING INFORMATION

Additional supporting information may be found in the online version of this article.

Figure S1. Near-infrared hyperspectral spectrum of the surface of grain A0159, acquired both at ISAS (Japan) and at IAS (France) using the MicrOmega instrument. The top image shows A0159 as imaged in the ISAS curation facility, while the images acquired after shipping at IAS are below, with carbonate-rich pixels indicated in red. The average grain surface spectra from both observations are compared in the top plot, and the spectrum of the carbonate-rich area is compared to those of dolomite and breunnerite identified in other Ryugu samples (C0108 and C0206). The stronger absorption observed between 2.8 and 3.2 μm in the spectra acquired at the IAS PTAL bench, compared to those from the ISAS curation facility, likely indicates water adsorption on the surface of grain A0159 during transport and handling.

Figure S2. Location of the two Xe-pFIB sections produced on sample A0159 and used in this work. A0159 was fixed onto an aluminum stub (Al-stub) using a piece of carbon tape (C-tape) which is represented schematically by two black and gray rectangles. Cut1 (*Pangea*) and Cut2 sections are not completely parallel to the Al-stub, as uneven beam ablation led to asymmetric material removal and a resulting tilt. Surrounding A0159 and adhered to the C-tape are other fragments, likely detached from the grain after fixation, as well as a dust particle.

Figure S3. Selection of the carbonate component (in red) on the CT image slice 0475 from ImageJ software using (a) a broader interval LAC = [5–7.25] and (b) a narrower interval LAC = [5.75–6.5]. The white arrows indicate the carbonate vein detected on A0159 surface by FTIR.

Figure S4. (a) BSE images highlighting the diversity in shape of opaque minerals. (b) BSE image of the OM-rich rectangular (circled in red) objects observed in *Pangea* section located in a matrix enriched in sub-micrometer sulfides. (c) A color composition close-up of *Pangea* section in which the phosphor (P)-rich grain is shown embedded in the dolomite vein. Ca, Si, Fe, S, and P in red, green, blue, yellow, and pink, respectively. (a) and (c) Cg, coarse-grained phyllosilicates; Fg, fine-grained phyllosilicates; Mag, magnetite; Sulf, sulfide; P-rich, here, Ca-phosphate; Dol, dolomite.